Numerical Investigation of the Planar Velocity Antidynamo Theorem in a Sphere

A.A. Bachtiar [*] D.J. Ivers, R.W. James [†]

August 18, 2003

Abstract

The Earth's main magnetic field is generally believed to be due to a dynamo process in the Earth's fluid outer core. A variety of antidynamo theorems exist that define conditions under which a magnetic field cannot be indefinitely maintained by dynamo actions against ohmic decay. One such theorem, the *Planar Velocity Antidynamo Theorem*, precludes field maintenance when the flow is everywhere parallel to some plane, e.g. the equatorial plane. This paper shows that the proof of the Planar Velocity Theorem fails when the flow is confined to a finite volume, so that then the theorem reverts to a conjecture. The paper also formulates the toroidal-poloidal spectral form of the magnetic induction equation for planar flows, as a basis for a numerical investigation. We have thus numerically determined the magnetic fields induced by various planar flows in spheres. In all but one flow the induced magnetic field has been found to decay in time, supporting a planar velocity conjecture. However one model is suggestive that field growth may occur. These results highlight the need for a mathematical proof of the conjecture, or alternatively, the determination of a functioning planar velocity dynamo.

1 Introduction

The Earth's main magnetic field exhibits behaviour on timescales ranging from seconds to millennia. Characteristics over longer timescales of $10 - 10^8$ years include secular variation, polar wandering, polarity reversals, and long term maintenance. The dynamo hypothesis, that such large scale behaviour is due to MHD interactions in the Earth's fluid core, is due to Larmor [16]. The feasibility of this hypothesis has been well established by numerous numerical kinematic and dynamic investigations, and the establishment of dynamical benchmark computer codes [3], [6], [5].

However, from almost the beginning of dynamo theory, so-called antidynamo theorems have hindered the construction of simple models based on laminar flows. Such theorems rule out magnetic field maintenance when certain simplifying geometric constraints are imposed either on the flow or the magnetic field. The known theorems where the constraints are in terms of spherical coordinates (r, θ, ϕ), are

[*]Department of Mathematics, University of Indonesia

[†]School of Mathematics & Statistics, University of Sydney, NSW 2006, Australia.
mailto:ronj@maths.usyd.edu.au

1. *Cowling's theorem*: This rules out the maintenance of an axisymmetric magnetic field $\mathbf{B}$ by an incompressible flow. It may be extended to an *Axisymmetric Theorem* (AT) that holds in quite general conditions [7], including compressible flow and non-uniform electrical conductivity.

2. *The Toroidal Velocity Theorem* (TVT): This rules out field maintenance by a purely toroidal fluid velocity $\mathbf{v}$, where $\mathbf{v} = \nabla \times (t\,\mathbf{r})$ for some defining scalar t. The TVT can be extended to the *Non-Radial Velocity Theorem* (NRVT), that precludes maintenance of a magnetic field by flows where $v_r = 0$ but $\nabla \cdot \mathbf{v} \not\equiv 0$ [9].

3. *The Radial Velocity Theorem* (RVT): The RVT rules out maintenance by radially symmetric flows $\mathbf{v} = v_r(r,t)\mathbf{e}_r$ [18], [8]. An offshoot of the TVT and RVT is the *Symmetric Velocity Theorem* (SVT) which rules out field maintenance by flows of the form $v_r(r,t)\mathbf{e}_r + \mathbf{v}_\mathrm{T}$ where $\nabla \cdot \mathbf{v} = \mathbf{v}_\mathrm{T} \cdot \mathbf{e}_r = 0$ [10]. The SVT does not supersede the RVT or TVT since the senses of decay are mathematically different.

4. *The Toroidal Field Theorem* (TFT): This precludes the maintenance of a purely toroidal magnetic field $\mathbf{B} = \nabla \times (T\mathbf{r})$ [14].

It is notable that there is no poloidal analog to the TVT, i.e. a magnetic field may be maintained by a purely poloidal flow [17]. However, a partial result has been established towards proving a poloidal analog of the TFT, in that it has been shown under certain assumptions that a purely poloidal magnetic field can not be maintained [13].

Various analogous results exist in cartesian coordinates. Cowling's Theorem corresponds to a 2-dimensional theorem, where a magnetic field B independent of one cartesian coordinate is ruled out [4]. And the TVT corresponds to a *Planar Velocity Theorem* (PVT) which precludes maintenance of $\mathbf{B}$ by incompressible flow with no z-component, i.e.

$$\mathbf{v} = \nabla \times (f\mathbf{e}_z)\,. \tag{1}$$

The conditions under which the PVT holds are central for this paper. In §2.2 it will be argued that a proof for the PVT has not been established when the conducting fluid volume is a sphere, the context of primary interest in rotating bodies such as the Earth. In §3.1 we derive toroidal-poloidal spectral equations, to be used later in §5 for a numerical investigation of specific planar velocity models.

2 The Planar Velocity Theorem

In this section we consider two cases: (a) where the conducting fluid occupies all space V_∞, and (b) where the fluid occupies a spherical volume V, of radius a and surface Σ, surrounded by free space $\widehat{V}$. The fluid is assumed to have constant electric conductivity σ, and magnetic diffusivity $\eta = 1/(\mu\sigma)$ where μ is the free space permeability.

For prescribed fluid velocity $\mathbf{v}$, the magnetic field $\mathbf{B}$ evolves according to

$$\frac{\partial \mathbf{B}}{\partial t} = \nabla \times (\mathbf{v} \times \mathbf{B}) + \eta \nabla^2 \mathbf{B}\ ,\ \text{in } V\ , \tag{2a}$$

$$\nabla \times \mathbf{B} = \mathbf{0}\ ,\ \text{in } \widehat{V}\ . \tag{2b}$$

2.1 The PVT for an Infinite Fluid

Suppose the fluid occupies all space, that $\mathbf{v}\cdot\mathbf{e}_z = 0$, and that $\mathbf{v}$ and $\mathbf{B}$ decrease sufficiently fast as $r \to \infty$, as detailed below. Then either $\mathbf{B} \equiv 0$, or $\mathbf{B}$ decays as $t \to \infty$. The details of the sense of decay are given in the following proof, derived from that of Zel'dovich and Ruzmaikin [22].

The z-component of (2a) is

$$\frac{\partial B_z}{\partial t} = -\mathbf{v}\cdot\nabla B_z + \eta\nabla^2 B_z, \tag{3}$$

Applying the divergence theorem yields

$$\frac{\partial}{\partial t}\int_V \frac{B_z^2}{2}\,dV = -\int_\Sigma (\mathbf{v}\frac{B_z^2}{2})\cdot\,\mathbf{d\Sigma} + \eta\int_\Sigma (B_z\nabla B_z)\cdot\,\mathbf{d\Sigma} - \eta\int_V (\nabla B_z)^2\,dV\ , \tag{4}$$

where $\mathbf{d\Sigma} = d\Sigma\mathbf{e}_r = r^2\sin\theta\,d\theta\,d\phi\,\mathbf{e}_r$ is the outward directed surface differential. Letting $a \to \infty$ gives

$$\frac{\partial}{\partial t}\int_{V_\infty} \frac{B_z^2}{2}\,dV = -\eta\int_{V_\infty} (\nabla B_z)^2\,dV\ \le\ 0\ , \tag{5}$$

assuming $\mathbf{v}B_z^2$, $B_z\nabla B_z$ are $\mathrm{o}(1/r^2)$ as $r \to \infty$. Then, either $B_z \equiv 0$, or $\|B_z\|_2 = \sqrt{\big(\int_{V_\infty} B_z^2\,dV\big)}$ decays strictly monotonically with t.

To show decay of B_x, B_y, introduce scalars ϕ, Φ, such that

$$B_x = \frac{\partial\Phi}{\partial y} + \frac{\partial\phi}{\partial x}\ , \qquad B_y = -\frac{\partial\Phi}{\partial x} + \frac{\partial\phi}{\partial y}\ .$$

Letting $\nabla_{\mathrm{h}}^2 \equiv \partial^2/\partial x^2 + \partial^2/\partial y^2$, $\nabla\cdot\mathbf{B} = 0$ implies

$$\nabla_{\mathrm{h}}^2\,\phi = -\frac{\partial B_z}{\partial z}\ ,$$

and hence

$$\phi = -\frac{1}{2\pi}\int \log|\mathbf{r}-\mathbf{r}'|\left(\frac{\partial B_z}{\partial z}\right)'\,dx'\,dy'\ , \tag{6}$$

where the integral is over a plane with $z' = z$ fixed. From (6) one infers that $\phi \equiv 0$ or decays as $t \to \infty$, following the behaviour of B_z. So asymptotically as $t \to \infty$, $\mathbf{B} = \nabla\times(\Phi\mathbf{e}_z)$. For this $\mathbf{B}$, uncurling (2a) yields

$$\frac{\partial\Phi}{\partial t} = -(\mathbf{v}\cdot\nabla\Phi) + \eta\nabla^2\Phi + \frac{\partial\psi}{\partial z}\ , \tag{7}$$

where $\psi = \psi(z,t)$. Let $\overline{\Phi}(\varpi, z) := (1/A)\int_A \Phi\,dA$ where the average is over the disc A of radius ϖ, at fixed z. Averaging (7), and applying the divergence theorem in the plane, yields

$$\frac{\partial\overline{\Phi}}{\partial t} = \frac{1}{A}\int_C \left(\eta\frac{\partial\Phi}{\partial\varpi} - v_\varpi\Phi\right)dC + \eta\,\frac{\partial^2\overline{\Phi}}{\partial z^2} + \frac{\partial\psi}{\partial z}\ , \tag{8}$$

where the line integral is around the perimeter C of A. Since Φ can be adjusted by adding a function of z without affecting $\mathbf{B}_{\mathrm{h}}$, we may take $\overline{\Phi}(\infty, z) = 0$. Letting $\varpi \to \infty$ in (8) then shows that $\partial\psi/\partial z \equiv 0$. Assuming $\mathbf{v}\Phi^2$, $\Phi\nabla\Phi$ are $\mathrm{o}(1/r^2)$ as $r \to \infty$, applying the divergence theorem to (7) implies

$$\frac{\partial}{\partial t}\int_{V_\infty} \Phi^2\,dV = -\eta\int_{V_\infty} (\nabla\Phi)^2\,dV\ .$$

Thus $\Phi \equiv 0$ or $\|\Phi\|_2$ decays strictly monotonically.

2.2 Failure of the PVT for a conducting sphere

The PVT is commonly thought to apply when the conducting fluid is confined to a finite volume (e.g. [19].) To consider this, let $(\cdots)^{\pm}$ represent values on the inside $(-)$ and outside $(+)$ of Σ, and $[\cdots]^{+}_{-} = (\cdots)^{+} - (\cdots)^{-}$ represent the jump across Σ.

If the boundary is fixed, $v_r = 0$ at $r = a$. In this case, (4) reduces to

$$\frac{\partial}{\partial t}\int_V \frac{B_z^2}{2}\,dV = \eta\int_\Sigma (B_z\nabla B_z)^-\cdot\,\mathbf{d\Sigma} - \eta\int_V (\nabla B_z)^2\,dV\ . \tag{9}$$

Since the current sources are confined to V, then $B_z = \mathcal{O}(1/r^3)$ as $r\to\infty$. Applying the divergence theorem, the z-component of (2b) yields

$$\int_{\widehat{V}} (\nabla B_z)^2\,dV = \int_\Sigma (B_z\nabla B_z)^+\cdot\mathbf{d\Sigma}\ . \tag{10}$$

Combining (9), (10), and using the continuity of B_z across Σ, leads to

$$\frac{\partial}{\partial t}\int_V \frac{B_z^2}{2}\,dV = -\eta\int_\Sigma B_z\left[\frac{\partial B_z}{\partial r}\right]^+_-\,d\Sigma - \eta\int_{V_\infty}(\nabla B_z)^2\,dV\ . \tag{11}$$

In general $\partial B_z/\partial r$ is discontinuous across Σ. The first term on the RHS of (11) therefore prevents a conclusion about the decay of B_z. The initial-value problem defined by (2), with initial value $\mathbf{B} = \mathbf{B}(\mathbf{r},0)$, has a unique solution if $\mathbf{B}$ is continuous across Σ. To impose continuity on $\partial B_z/\partial r$ would in general result in that initial-value problem being over-determined, with no solution.

All antidynamo theorems summarized in §1 rely on the induction equation (2a) decoupling somehow. In the PVT of §2.1, the induction equation for B_z has decoupled so that there is no generation of B_z from the horizontal component $\mathbf{B}_\mathrm{h}$, and B_z decays, if not identically zero. This decoupling depends on $v_z = 0$, and η being constant in V_∞. Introducing the boundary $r = a$ as in §2.2 has introduced variable η, and allowed diffusive coupling between B_z from $\mathbf{B}_\mathrm{h}$ at the boundary. An alternative view is obtained by considering continuity conditions across Σ, and rewriting $[\partial B_z/\partial r]^+_-$ in terms of the electric current density $\mathbf{j} = \mu^{-1}\nabla\times\mathbf{B}$. Since $\nabla\cdot\mathbf{B} = 0$ implies $[\partial B_r/\partial r]^+_- = 0$, then

$$\left[\frac{\partial B_z}{\partial r}\right]^+_- = \left[\frac{\partial}{\partial r}\left(B_r\cos\theta - B_\theta\sin\theta\right)\right]^+_- = -\sin\theta\left[\frac{\partial B_\theta}{\partial r}\right]^+_-\ .$$

Also, since $[\partial B_r/\partial\theta]^+_- = 0$, and $j^+_\phi = 0$,

$$\mu j^-_\phi = \frac{1}{r}\left(\frac{\partial(rB_\theta)}{\partial r} - \frac{\partial B_r}{\partial\theta}\right)^- = \frac{1}{r}\left(\frac{\partial(rB_\theta)}{\partial r}\right)^- - \frac{1}{r}\left(\frac{\partial B_r}{\partial\theta}\right)^+ = -\left[\frac{\partial B_\theta}{\partial r}\right]^+_-\ .$$

So the coupling term on the RHS of (11) is

$$\eta\int_\Sigma B_z\left[\frac{\partial B_z}{\partial r}\right]^+_-\,d\Sigma = \frac{1}{\sigma}\int_\Sigma \sin\theta\, j^-_\phi\, B_z\,d\Sigma = \frac{1}{\sigma}\int_{\Sigma^-}\sin\theta\, j_\phi\, B_z\,d\Sigma\ . \tag{12}$$

The presence of the boundary $r = 1$ must promote the existence of tangential currents, generally with a j_ϕ component. So the coupling term may be significant. However B_z on Σ is an integrated contribution from $\mathbf{j}$ throughout V. So the sign of (12) is unknown. If the sign is negative, then (12) may act as a generation term in (11). Given the lack of a proof of decay in the present case, we therefore investigate numerical solutions to see if growing magnetic fields can be found.

3 Numerical Methods

The non-dimensionalized form of the induction equation (2a) is

$$\frac{\partial \mathbf{B}}{\partial t} = R\nabla \times (\mathbf{v} \times \mathbf{B}) + \nabla^2 \mathbf{B} \; . \tag{13}$$

Here R=UL/η is the Reynolds number, based on characteristic speed U and length L, with t measured on the diffusion time scale L^2/η. For the angular coordinates θ, ϕ, we employ a spherical harmonic spectral representation as described in §3.1. For solution of the resulting radial equations we employ both finite differences and Chebyshev collocation as described in §3.3.

3.1 The Spherical Harmonic Spectral Equations

We represent $\mathbf{B}$ and $\mathbf{v}$ in poloidal–toroidal formalism, using scalars S, T and s, t respectively:

$$\mathbf{B} = \nabla \times (\mathbf{r}\, T) + \nabla \times (\nabla \times \mathbf{r}\, S) \; , \tag{14}$$

$$\mathbf{v} = \nabla \times (\mathbf{r}\, t) \; + \nabla \times \times (\nabla \times \mathbf{r}\, s) \; ; \tag{15}$$

and expand these scalars in spherical harmonics,

$$T = \sum_{n,m} T_n^m Y_n^m \; , \qquad S = \sum_{n,m} S_n^m Y_n^m \; , \qquad t = \sum_{n,m} t_n^m Y_n^m \; , \qquad s = \sum_{n,m} s_n^m Y_n^m \; , \tag{16}$$

where $m = -n, \ldots, n$ and $n = 1, 2, 3, \ldots$. We denote the individual vector modes of $\mathbf{B}$ by $\mathbf{T}_n^m = \nabla \times (\mathbf{r}\, T_n^m Y_n^m)$, $\mathbf{S}_n^m = \nabla \times (\nabla \times \mathbf{r}\, S_n^m Y_n^m)$, and similarly for $\mathbf{v}$, $\mathbf{t}_n^m$, $\mathbf{s}_n^m$.

In the above,

$$Y_n^m = (-)^m \overline{Y_n^{-m}} = (-)^m \left[\frac{2n+1}{2-\delta_m^0} \right]^{\frac{1}{2}} P_n^m(\cos\theta) e^{im\phi} \; , \tag{17}$$

where

$$P_n^m(\mu) = \left[\frac{(2-\delta_m^0)(n-m)!}{(n+m)!} \right]^{\frac{1}{2}} \frac{(1-\mu^2)^{m/2}}{2^n n!} \left[\frac{d}{d\mu} \right]^{n+m} (\mu^2 - 1)^n \tag{18}$$

is the Schmidt-normalized Legendre function. The overbar $\overline{(\cdots)}$ denotes complex conjugate, and δ_m^0 is the Kronecker delta. Since $\mathbf{B}$ and $\mathbf{v}$ are real, (17) implies that

$$S_n^{-m} = (-)^m \overline{S_n^m} \; , \qquad T_n^{-m} = (-)^m \overline{T_n^m} \; , \tag{19}$$

and similarly for s_n^m and t_n^m .

With m-superscripts suppressed, and $D_n \equiv \partial^2/\partial r^2 + (2/r)\partial/\partial r - n(n+1)/r^2$, the spectral form of (13) is

$$\left(\frac{\partial}{\partial t} - D_{n_3} \right) S_{n_3} = R \sum_{n_1,n_2} \left[(s_{n_1} S_{n_2} S_{n_3}) + (s_{n_1} T_{n_2} S_{n_3}) + (t_{n_1} S_{n_2} S_{n_3}) \right] \; , \tag{20}$$

$$\left(\frac{\partial}{\partial t} - D_{n_3} \right) T_{n_3} = R \sum_{n_1,n_2} \left[(s_{n_1} S_{n_2} T_{n_3}) + (s_{n_1} T_{n_2} T_{n_3}) \right.$$
$$\left. + (t_{n_1} S_{n_2} T_{n_3}) + (t_{n_1} T_{n_2} T_{n_3}) \right] \; . \tag{21}$$

There is no interaction $(t_{n_1}T_{n_2}S_{n_3})$ in (20) since a poloidal magnetic field can not be created by the interaction of a toroidal flow and toroidal field. The original Bullard-Gellman formalism [1] differs from the present formalism, so details of the interaction terms in (20), (21) are given below. With $p_1 := n_1(n_1+1)$ and $q_1 := p_1 - p_2 - p_3$ etc,

$$(s_{n_1}S_{n_2}S_{n_3}) = \Big\{ \big[q_3(p_2-p_1)\frac{s_{n_1}}{r^2} - p_2q_2\frac{s'_{n_1}}{r}\big]S_{n_2} + p_1q_1\frac{s_{n_1}}{r}S'_{n_2}\Big\}\frac{(-)^{m_3}A}{8\pi p_3}\ , \tag{22}$$

$$(s_{n_1}T_{n_2}S_{n_3}) = \frac{p_1}{4\pi r p_3}(-)^{m_3}E\, s_{n_1}T_{n_2}\ , \tag{23}$$

$$(t_{n_1}S_{n_2}S_{n_3}) = \frac{p_2}{4\pi r p_3}(-)^{m_3}E\, t_{n_1}S_{n_2}\ , \tag{24}$$

$$(s_{n_1}S_{n_2}T_{n_3}) = \Big\{ \big[(p_1+p_2+p_3)\frac{s_{n_1}}{r^3} + q_3\frac{s'_{n_1}}{r^2} - p_2\frac{s''_{n_1}}{r}\big]S_{n_2} + q_3\big(\frac{s_{n_1}}{r^2}+\frac{s'_{n_1}}{r}\big)S'_{n_2} - p_1\frac{s_{n_1}}{r}S''_{n_2}\Big\}\frac{(-)^{m_3}E}{4\pi p_3}\ , \tag{25}$$

$$(s_{n_1}T_{n_2}T_{n_3}) = \Big\{ \big[p_3q_3\big(\frac{s_{n_1}}{r^2}+\frac{s'_{n_1}}{r}\big) + p_1q_1\frac{s'_{n_1}}{r}\big]T_{n_2} + p_1q_1\frac{s_{n_1}}{r}T'_{n_2}\Big\}\frac{(-)^{m_3}A}{8\pi p_3}\ , \tag{26}$$

$$(t_{n_1}S_{n_2}T_{n_3}) = \Big\{ \big(p_3q_3\frac{t_{n_1}}{r^2} + p_2q_2\frac{t'_{n_1}}{r}\big)S_{n_2} + (p_2q_2+p_3q_3)\frac{t_{n_1}}{r}S'_{n_2}\Big\}\frac{(-)^{1+m_3}A}{8\pi p_3}\ , \tag{27}$$

$$(t_{n_1}T_{n_2}T_{n_3}) = \frac{(-)^{m_3}}{4\pi r}E\, t_{n_1}T_{n_2}\ . \tag{28}$$

In (22)–(28), $S' \equiv \partial S/\partial r$ etc; and

$$A = \int_{4\pi} Y_{n_1}^{m_1}Y_{n_2}^{m_2}Y_{n_3}^{-m_3}\sin\theta\, d\theta\, d\phi\ , \tag{29}$$

$$E = \int_{4\pi}\left(\frac{\partial Y_{n_1}^{m_1}}{\partial\theta}\frac{\partial Y_{n_2}^{m_2}}{\partial\phi} - \frac{\partial Y_{n_1}^{m_1}}{\partial\phi}\frac{\partial Y_{n_2}^{m_2}}{\partial\theta}\right)Y_{n_3}^{-m_3}\, d\theta\, d\phi\ . \tag{30}$$

are Adams and Elsasser coupling integrals, which can be evaluated using Wigner coefficients [11].

Equations (22)–(28) are solved subject to the conditions

$$S_n = T_n = 0\ , \quad \text{at } r = 0\ , \tag{31}$$

$$\frac{\partial S_n}{\partial r} + (n+1)S_n = T_n = 0\ , \quad \text{at } r = 1\ . \tag{32}$$

The velocity satisfies

$$s_n = t_n = 0\ , \quad \text{at } r = 0\ , \tag{33}$$

$$s_n = 0\ , \quad \text{at } r = 1\ , \tag{34}$$

and sometimes

$$t_n = \frac{\partial s_n}{\partial r} = 0\ , \quad \text{at } r = 1\ . \tag{35}$$

Equations (31) and (33) are required for differentiability of $\mathbf{B}$ and $\mathbf{v}$ with respect to x, y, z at $r = 0$. Equations (32) reflect the continuity of $\mathbf{B}$ across Σ and the current-free nature of $\widehat{V}$. Equations (34) and (35) apply for a fixed boundary and no slip respectively.

3.2 Selection Rules and Field Decoupling

The A and E integrals in (29), (30) impose various selection rules [11] on the interaction terms in (22)–(28):

SR1: $(s_{n_1} S_{n_2} S_{n_3})$, $(s_{n_1} T_{n_2} T_{n_3})$, and $(t_{n_1} S_{n_2} T_{n_3})$ depend on A and are zero unless $n_1 + n_2 + n_3$ is even, and $|n_1 - n_2| \le n_3 \le n_1 + n_2$.

SR2: $(s_{n_1} T_{n_2} S_{n_3})$, $(s_{n_1} S_{n_2} T_{n_3})$, $(t_{n_1} S_{n_2} S_{n_3})$, and $(t_{n_1} T_{n_2} T_{n_3})$ depend on E and are zero unless $n_1 + n_2 + n_3$ is odd, and $|n_1 - n_2| < n_3 < n_1 + n_2$.

SR3: $(s_{n_1} S_{n_2} S_{n_3}), \ldots, (t_{n_1} T_{n_2} T_{n_3})$ are all zero unless $m_3 = m_1 + m_2$.

For the present purposes it is convenient to classify the fields $\mathbf{v}$ and $\mathbf{B}$ as having dipole (D) or quadrupole (Q) parity if their poloidal and toroidal components belong to one of the following chains:-

$$\begin{aligned} \text{D:}\quad & S_1^0\,, S_1^1\,, T_2^0\,, T_2^1\,, T_2^2\,, S_3^0\,, S_3^1\,, S_3^2\,, S_3^3\,, T_4^0\,, T_4^1\,, T_4^2\,, T_4^3\,, T_4^4\,, \ldots \\ \text{Q:}\quad & T_1^0\,, T_1^1\,, S_2^0\,, S_2^1\,, S_2^2\,, T_3^0\,, T_3^1\,, T_3^2\,, T_3^3\,, S_4^0\,, S_4^1\,, S_4^2\,, S_4^3\,, S_4^4\,, \ldots \end{aligned} \tag{36}$$

Here, S_n^m denotes the presence of both S_n^m and S_n^{-m} and similarly for T. The D chain comprises S-harmonics with odd n, and T-harmonics with even n; the Q chain comprises S-harmonics with even n, and T-harmonics with odd n .

Rules SR1 and SR2 imply that if $\mathbf{v}$ has Q-parity, then $\mathbf{B}$ decouples into independent chains, a D chain, and a Q chain. This decoupling greatly reduces the size of the matrices in the computations described in §3.3. The decoupling is verified by considering the interactions shown in Table 1 on the next page, where **bold** entries show the type of harmonic produced by the various interactions. For example, $(s_{n_1} S_{n_2} S_{n_3})$ must satisfy SR1, so is zero unless $n_1{+}n_2{+}n_3$ is even. Thus, a Q-parity $\mathbf{s_{n_1}}$ interacts with a D-parity $\mathbf{S_{n_2}}$ from chain D to produce a D-parity $\mathbf{S_{n_3}}$ also in chain D. However a D-parity $\mathbf{s_{n_1}}$ interacts with a D-parity $\mathbf{S_{n_2}}$ from chain D to produce a Q-parity $\mathbf{S_{n_3}}$ that is not in chain D. Similar considerations lead to the chain-preserving interactions shown asterisked in Table 1, and show that Q-parity s_n, t_n preserve chains D and Q, whereas D-parity s_n, t_n destroy chains D and Q.

Independently of D-Q decouplings, the field can also be decoupled with respect to the order m, using SR3. Suppose $\mathbf{v}$ only contains harmonics with orders m_1 chosen from the set $\{m : m = 0 \bmod k\}$ for some integer k. Then, allowing for $\pm$ m-pairs as required by (19), SR3 implies that $\mathbf{B}$ decouples into independent chains containing harmonics with orders m_2, m_3 chosen from one of the sets $\mathrm{M}_{\ell k} := \{m : \ m = \ell \bmod k, \text{ or } m = (k - \ell) \bmod k\}$, $\ell = 1, 2, \ldots$. For example, if

		S_{n_3}				T_{n_3}			
		S_{n_2}		T_{n_2}		S_{n_2}		T_{n_2}	
		Odd D	Even Q	Odd Q	Even D	Odd D	Even Q	Odd Q	Even D
s_{n_1}	Odd D	**Even Q**	**Odd D**	**Odd D**	**Even Q**	**Odd Q**	**Even D**	**Even D**	**Odd Q**
	Even Q	**Odd D***	**Even Q***	**Even Q***	**Odd D***	**Even D***	**Odd Q***	**Odd Q***	**Even D***
t_{n_1}	Odd Q	**Odd D***	**Even Q***	Always zero		**Even D***	**Odd Q***	**Odd Q***	**Even D***
	Even D	**Even Q**	**Odd D**	Always zero		**Odd Q**	**Even D**	**Even D**	**Odd Q**

Table 1: Toroidal and Poloidal Interactions.

$m_1 = 4$, there are three decoupled **B**-chains:

$$\begin{aligned}
&\mathrm{M}_{04} : m = 0 \bmod 4 : && S_1^0\,, T_1^0\,, S_2^0\,, T_2^0\,, S_3^0\,, T_3^0\,, S_4^0\,, S_4^4\,, T_4^0\,, T_4^4\,,\\
& && S_5^0\,, S_5^4\,, T_5^0\,, T_5^4\,, S_6^0\,, S_6^4\,, T_6^0\,, T_6^4\,, \ldots\\
&\mathrm{M}_{14} : m = (1\,\mathrm{or}\,3) \bmod 4 : && S_1^1\,, T_1^1\,, S_2^1\,, T_2^1\,, S_3^1\,, S_3^3\,, T_3^1\,, T_3^3\,, S_4^1\,, S_4^3\,,\\
& && T_4^1\,, T_4^3\,, S_5^1\,, S_5^3\,, S_5^5\,, T_5^1\,, T_5^3\,, T_5^5\,, \ldots\\
&\mathrm{M}_{24} : m = 2 \bmod 4 : && S_2^2\,, T_2^2\,, S_3^2\,, T_3^2\,, S_4^2\,, T_4^2\,, S_3^2\,, T_4^2\,, S_4^2\,, T_4^2\,,\\
& && S_5^2\,, T_5^2\,, S_5^4\,, T_5^4\,, S_6^2\,, T_6^2\,, S_6^4\,, T_6^4\,, S_6^6\,, T_6^6\,, \ldots
\end{aligned}$$

Combining this m-decoupling with the D-Q decoupling in (36) further significantly reduces the dimensions of the computational problem. We will denote such chains $\mathrm{DM}_{\ell k}$ or $\mathrm{QM}_{\ell k}$.

3.3 The Radial Equations

For **v** stationary, **B** can be represented as a superposition of discrete modes:

$$\mathbf{B} = \sum_{\lambda} \mathbf{B}_\lambda\, e^{\lambda t}\ .$$

To find whether non-decaying modes exist we need to determine $\max_\lambda \Re\{\lambda\}$. Having formed the spectral equations (20), (21), we truncate the series (16) at some finite degree N. To validate results we adopted a variety of numerical approaches for discretizing the radial direction: (a) 2^{nd}-order finite-difference approximations, (b) 4^{th}-order finite differences, and (c) Chebyshev collocation. Method (a) was sometimes supplemented by Richardson extrapolation to give about the same accuracy as method (b). Several independent computer programs were used, one based directly on the spectral equations (22)–(28), and another using a Wigner coefficient form of the spectral equations [12]. Results from all methods agreed satisfactorily.

For methods (a),(b) the range $0 \le r \le 1$ was divided into J equal subintervals with grid points $r_j = jh$, $(j = 0 : J)$. Difference approximations were applied to the truncated poloidal and toroidal spectral equations (20),(21) at $j{=}1 : J{-}1$, and to the poloidal equation at $j = J$.

For (a), centred-difference formulas were used for $j = 1 : J - 1$. At the boundary the poloidal equation (20) was discretized in either of two ways:-

(i) with a centred formula for S_n'' using an external point r_{J+1} , where S_n there was eliminated by a centred difference approximation to the poloidal boundary condition (32a);

(ii) with the non-centred formula

$$f_0^{(2)} = \frac{-f_{-2} + 8f_{-1} - 7f_0 + 6hf_0^{(1)}}{2h^2} + \frac{1}{6}f^{(4)}(\eta)h^2 \,, \tag{37}$$

for $f = S_n''$, where $f_0^{(1)} = -(n+1)f_0$ by the poloidal boundary condition (32a).

Method (i) above is theoretically less accurate than (ii) since it introduces an $\mathcal{O}(h)$ term in the difference equation for S_n at $j = J$. However for $J \gtrsim 200$ no significant numerical difference was found. On the other hand, the non-centred formula (37) in method (ii) produces a matrix with a somewhat wider bandwidth, as shown by comparing Figures 1, 2, 3. All tables herein show results from method (i), and other methods were used as a check.

For (b), centred-difference formulas were applied at $j = 1 : J-2$. At $j = 1$, the symmetry property $f(-r) = (-)^n f(r)$ of $f = S_n$ and T_n, was used. For the points $j = J-1$ and $j = J$, non-centred formulas were used:-

$$f_0^{(1)} = \frac{-f_{-3} + 6f_{-2} - 18f_{-1} + 10f_0 + 3f_1}{12h} - \frac{1}{20}f^{(5)}(\eta)h^4$$
$$f_0^{(2)} = \frac{f_{-4} - 6f_{-3} + 14f_{-2} - 4f_{-1} - 15f_0 + 10f_1}{12h^2} - \frac{13}{180}f^{(6)}(\eta)h^4$$

for $f = T_n$ at $j = J-1$, where $f_1 = 0$ by boundary condition (32b);

$$f_0^{(1)} = \frac{f_{-2} - 9f_{-1} - 9f_0 + 17f_1 - 6hf_1^{(1)}}{18h} + \frac{1}{60}f^{(5)}(\eta)h^4$$
$$f_0^{(2)} = \frac{3f_{-3} - 32f_{-2} + 252f_{-1} - 480f_0 + 257f_1 - 60hf_1^{(1)}}{144h^2} - \frac{1}{360}f^{(6)}(\eta)h^4$$

for $f = S_n$ at $j = J-1$, where $f_1^{(1)} = -(n+1)f_1$ by boundary condition (32a);

$$f_0^{(2)} = \frac{-9f_{-4} + 64f_{-3} - 216f_{-2} + 576f_{-1} - 415f_0 + 300hf_0^{(1)}}{72h^2} + \frac{1}{15}f^{(6)}(\eta)h^4$$

for $f = S_n$ at $j = J$, where $f_0^{(1)} = -(n+1)f_0$ by boundary condition (32a).

For method (c) expansions up to degree $2J$ containing Chebychev polynomials were used:

$$f_n^m(r) = \sum_{j=1}^{J} f_{j,n}^m r^q T_{2j-1}(r) \,, \qquad f = T, S \,, \tag{38}$$

where $q = 1$ if n is even or $q = 0$ if n is odd. The J collocation points $r_j = \cos(j\pi/2J)$, $j = 0 : J-1$ were used.

For a given magnetic Reynolds number R, each of the approaches (a),(b),(c), leads to an eigenvalue problem

$$\mathbf{A}\mathbf{x} = \lambda \mathbf{D}\mathbf{x} \,. \tag{39}$$

For methods (a),(b) $\mathbf{D}$ is the unit matrix, and for (c) $\mathbf{D}$ is a block-diagonal matrix with a block of the form $[r_i^q T_{2j-1}(r_i)]$ for each n.

Convergence was sought by increasing N, J. The solution of (39) was straightforward except that very large dimensions were required in some cases.

The matrix $\mathbf{A}$ is very sparse and banded. Moreover, the matrix band itself has mostly zero elements due to the selection rules given in §3.2 . This bandedness is shown in Figures 1–7 for the various radial discretization methods. Figures 2 and 3 show how the sparsity pattern varies with different orderings of the eigenvector, namely jnm ordering where m varies fastest, and jmn ordering where n varies fastest. These two orderings are near optimal in respect to minimizing the bandwidth of $\mathbf{A}$.

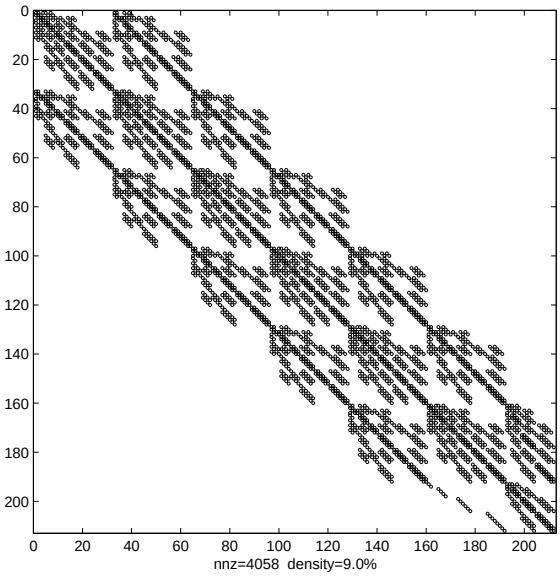

Figure 1: Banded matrix from the $\mathcal{O}(h^2)$ finite difference scheme with jnm-ordering.

To validate results, (39) was solved by various independent methods: (a) inverse iteration ([21] without pivoting, which preserves the bandwidth and allows higher truncation levels, (b) inverse iteration with partial pivoting at various thresholds, and (c) the implicitly restarted Arnoldi Method (from ARPACK) with reverse communication. Both MATLAB and in-house Fortran programs were used.

Plotting $\max_\lambda \Re\{\lambda\}$ against R allows us to infer whether $\Re\{\lambda\} > 0$ for any of the models of $\mathbf{v}$ in §5.

4 Planar flows in toroidal poloidal form

For the planar flow (1), the streamlines are the level surfaces of the stream function f, lying in planes parallel to the xy-plane. To apply the numerical methods of §3 we need to express $\mathbf{v}$ in the poloidal-toroidal forms (15), (16). Expanding $f = \sum f_n^m Y_n^m$, and dotting (1) with $\mathbf{r}$ gives

$$L^2 s_n^m Y_n^m = n(n+1) s_n^m Y_n^m = f_n^m \frac{\partial Y_n^m}{\partial \phi} \ ,$$

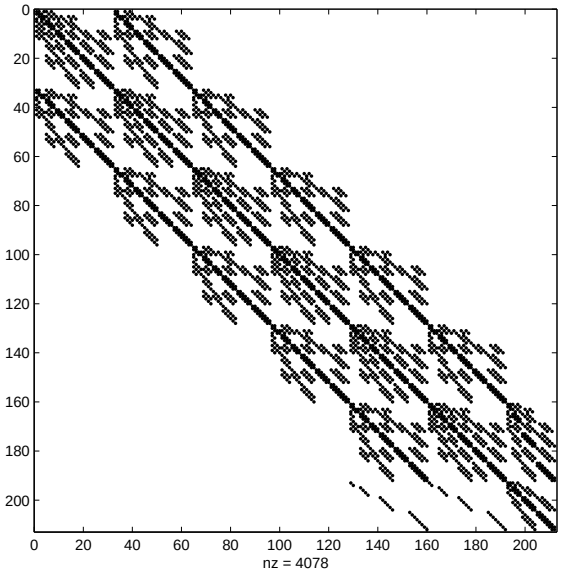

Figure 2: Banded matrix from the $\mathcal{O}(h^2)$ finite difference scheme with jnm-ordering and a higher accuracy difference approximation at the boundary.

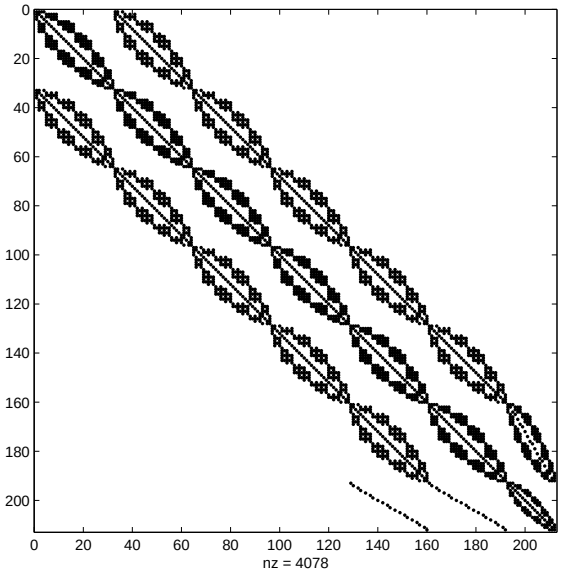

Figure 3: Banded matrix from the $\mathcal{O}(h^2)$ finite difference scheme with jmn-ordering.

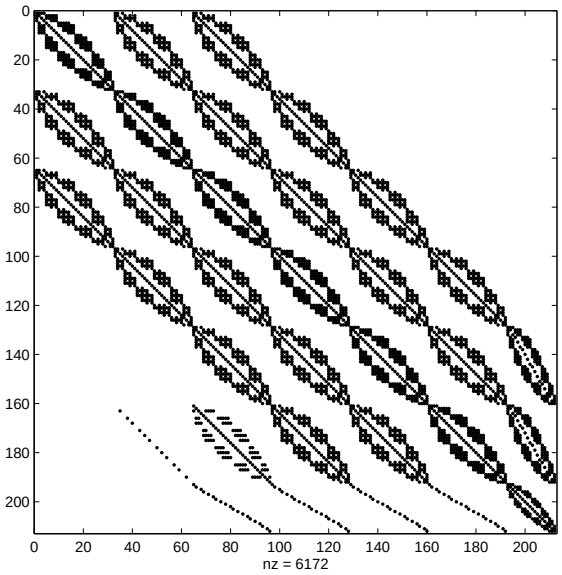

Figure 4: Banded matrix from the $\mathcal{O}(h^4)$ finite difference scheme with jmn-ordering.

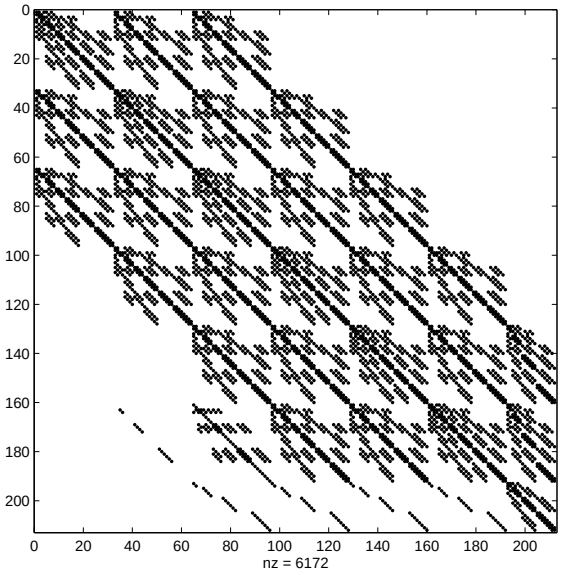

Figure 5: Banded matrix from the $\mathcal{O}(h^4)$ finite difference scheme with jnm-ordering.

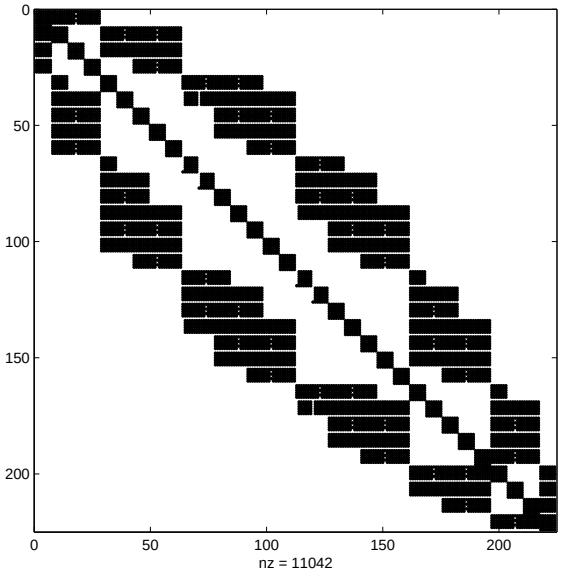

Figure 6: Banded matrix from the Chebychev spectral scheme with jnm-ordering.

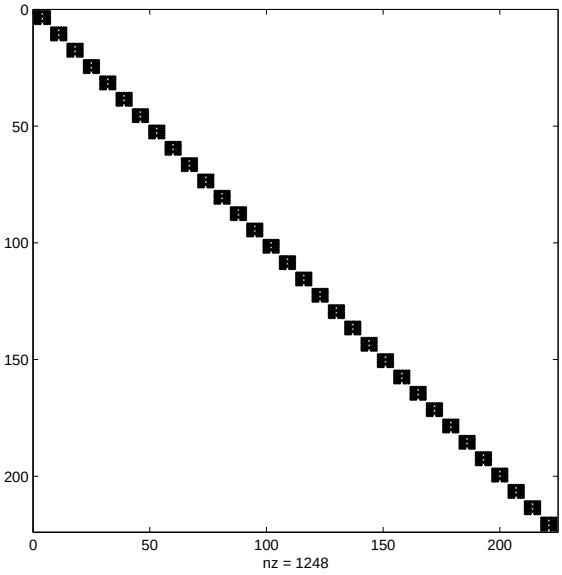

Figure 7: The RHS matrix from equation (39).

where $L^2 Y_n^m = -\frac{1}{\sin\theta}\Big[\frac{\partial}{\partial\theta}\big(\sin\theta\,\frac{\partial}{\partial\theta}\big) + \frac{\partial^2}{\partial\phi^2}\Big] Y_n^m = n(n+1)Y_n^m$. Thus

$$s_n^m = \frac{i\,m}{n(n+1)}\, f_n^m \ . \tag{40}$$

To obtain the toroidal coefficient t_n^m of the flow, we use the curl of (1):

$$\begin{aligned} L^2 t = \mathbf{r}\cdot\nabla\times\mathbf{v} &= \mathbf{r}\cdot\nabla\times(\nabla f\times\mathbf{e}_z) \\ &= -2\cos\theta\frac{\partial f}{\partial r} + \frac{\cos\theta}{r}L^2 f + \frac{\sin\theta}{r}\frac{\partial}{\partial\theta}\left(f - r\frac{\partial f}{\partial r}\right). \end{aligned} \tag{41}$$

With superscript m suppressed, and $\alpha_n := \sqrt{\big[(n^2-m^2)/(4n^2-1)\big]}$, the spherical harmonics defined by (17) satisfy recurrence relations [2]:

$$\begin{aligned} \cos\theta\, Y_n &= \alpha_{n+1}Y_{n+1} + \alpha_n Y_{n-1}\ , \\ \sin\theta\,\frac{\partial Y_n}{\partial\theta} &= n\alpha_{n+1}Y_{n+1} - (n+1)\alpha_n Y_{n-1}\ . \end{aligned}$$

Using these, and letting $d_n \equiv d/dr + n/r$, the spectral form of (41) is found to be

$$n(n+1)t_n = -(n+1)\alpha_n d_{1-n} f_{n-1} + n\alpha_{n+1} d_{n+2} f_{n+1}\ . \tag{42}$$

If f consists of only a single degree n, i.e.

$$f = f_n^m Y_n^m + f_n^{-m} Y_n^{-m} = 2\Re\{f_n^m Y_n^m\}\ , \tag{43}$$

then, from (42),

$$t_{n-1} = \frac{\alpha_n}{n}\, d_{n+1} f_n\ , \qquad\qquad t_{n+1} = -\frac{\alpha_{n+1}}{n+1}\, d_{-n} f_n\ . \tag{44}$$

More generally, for each f_n^m in the expansion $f = \sum f_n^m Y_n^m$, there will be one poloidal flow coefficient s_n^m given by (40), and two toroidal flow coefficients $t_{n\pm1}^m$ given by (44). So, for a flow derived from a prescribed f, it is straightforward to find the corresponding poloidal and toroidal coefficients. This approach will be the basis of our numerical investigation in §5.1.

It is of interest to consider the inverse problem. That is, is it possible to convert a given flow $\mathbf{v}$ to a planar flow, by addition of components defined via (40), (44)? We will use the terminology 'planarizing' for such a construction. Clearly, if $m \neq 0$, then for given $\mathbf{s}_n^m$, one can find f_n from (40), and construct $\mathbf{t}_{n\pm1}$ from (44). The combination $\mathbf{s}_n^m + \mathbf{t_{n-1}} + \mathbf{t_{n+1}}$ is then planar, and $\mathbf{s}_n^m$ has been planarized. However, to planarize a given $\mathbf{t}_n^m$ component, there are 2 paths one might follow. One has to find either (a) an f_{n+1} from (44a), or (b) an f_{n-1} from (44b). In (a) one generates a planarizing s_{n+1} from (40) and t_{n+2} from (44b). In (b) one generates the planarizing s_{n-1} from (40) and t_{n-2} from (44a). For given t_n, the f-solutions of (44) satisfying the differentiability condition (33) are

$$\text{(a) } f_{n+1} = \frac{n+1}{\alpha_{n+1}} r^{-n-2}\int_0^r r^{n+2}\, t_n\, dr\ , \quad \text{(b) } f_{n-1} = -\frac{n}{\alpha_n} r^{n-1}\int_0^r r^{-n+1}\, t_n\, dr\ .$$

Thus, to satisfy the fixed boundary condition at $r=1$, t_n must satisfy at least one of

$$\text{(a)}\quad \int_0^1 r^{n+2}\, t_n\, dr = 0\ , \qquad \text{(b)}\quad \int_0^1 r^{-n+1}\, t_n\, dr = 0\ . \tag{45}$$

If t_n satisfies (45a) then the corresponding planar flow is $\mathbf{t}_n + \mathbf{t}_{n+2} + \mathbf{s}_{n+1}$. If t_n satisfies (45b) then the corresponding planar flow is $\mathbf{t}_n + \mathbf{t}_{n-2} + \mathbf{s}_{n-1}$. If t_n satisfies neither of (45), then $\mathbf{t}_n^m$ cannot be planarized by this method.

Later, in §5.2, we illustrate these points by considering the possibility of planarizing some classic flows where $\mathbf{v}$ is defined by a set of s_n^m, t_n^m coefficients.

5 Results for various planar flows

In this section, we solve the kinematic dynamo problem comprising (20), (21), (31), (32), for various planar flows. First, we consider flows with a single harmonic degree, then some flows of historical interest.

5.1 Flows of One Harmonic Degree

With $p = 1, 2, 3, \ldots$, consider the stream function

$$f_n^m = r^n(1 - r^2)^p \ . \tag{46}$$

The associated planar flow is

$$\mathbf{v} = 2\Re\{\mathbf{s}_n^m + \mathbf{t}_{n+1}^m + \mathbf{t}_{n-1}^m\} \ , \tag{47}$$

where s_n^m, t_n^m are given by (40), (44). This flow satisfies the differentiability condition (33), the fixed boundary condition (34), the no-slip condition (35) if $p > 1$, and supports D-Q decoupling as in (36) if n is even.

Computer limitations restricted our investigation to relatively low values of n, m, p. Whilst some of the $\lambda_{\max}$ were found to be complex, representing an oscillatory magnetic field mode, in general this report omits the imaginary parts of $\lambda_{\max}$ since we are primarily interested in whether the field grows or not.

5.1.1 Cases $n = 2, 4$; $m = 0$

If $m = 0$, then $s_n^m = 0$ by (40). Figure 9 on the following page shows the streamlines, which are just circles in planes of constant z. Such purely toroidal flow is ruled out by the Toroidal Velocity Theorem of §1, with a theoretical decay rate upper bound $\lambda \leq -\pi^2$. These flows were used only as one of the computational checks. Here there is full decoupling with respect to the order $m_2 = m_3$ of the magnetic field, and one can independently investigate chains

$$S_1^{m_3}, T_2^{m_3}, S_3^{m_3}, T_4^{m_3}, \ldots$$

for various m_3. The λ-profile for $m_3 = 1$, shown in Figure 8, is typical for $m_3 \neq 0$. The figure shows agreement with the $-\pi^2$ bound on $\Re\{\lambda\}$, that the bound is only attained at $R_m = 0$, and that this particular mode is highly oscillatory for larger R_m. For $m_1 = m_2 = m_3 = 0$, the only non zero interaction amongst (22)–(28) is $(t_{n_1} S_{n_2} T_{n_3})$. So then the poloidal magnetic modes S_n^0 decay independently at the free decay rate for each S_n. In particular, S_1^0 decays at the slowest decay rate $-\pi^2$, and any magnetic field chain containing this mode will decay at that same rate, regardless of the choices for N, p, R. In this case our computations showed that $\pi^2 \approx 9.87$ was attained even for truncations as low as $J = 20$ — see Table 2 for results using the chain DM_{01} which contains all permissible m_3.

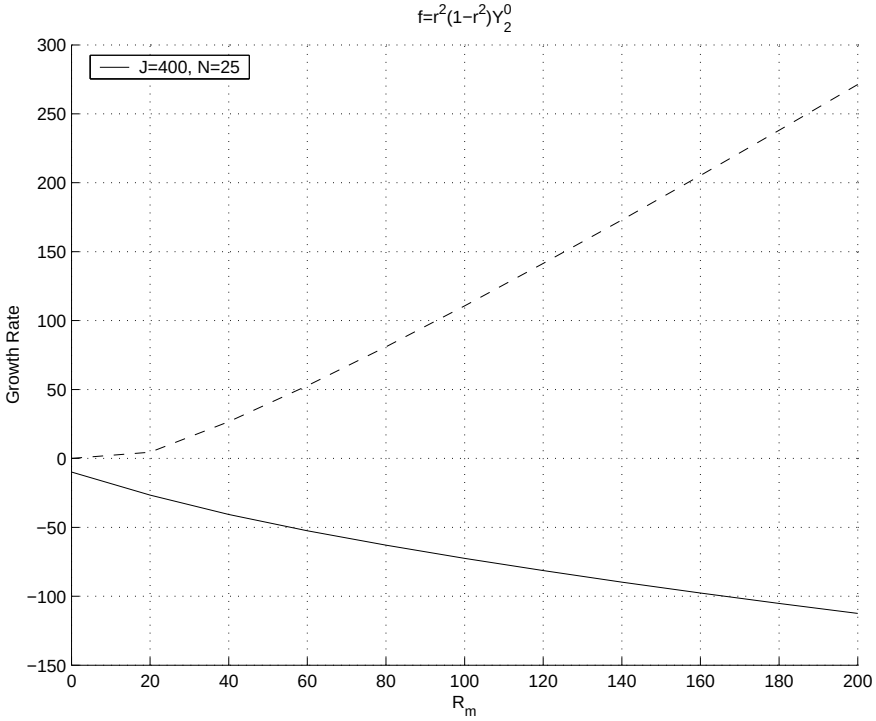

Figure 8: $\Re\{\lambda_{\max}\}$ (—) and $\Im\{\lambda_{\max}\}$ (- - -) for $n = 2$, $m = 0$, $p = 1$, $m_3 = 1$, $N = 25$, $J = 400$.

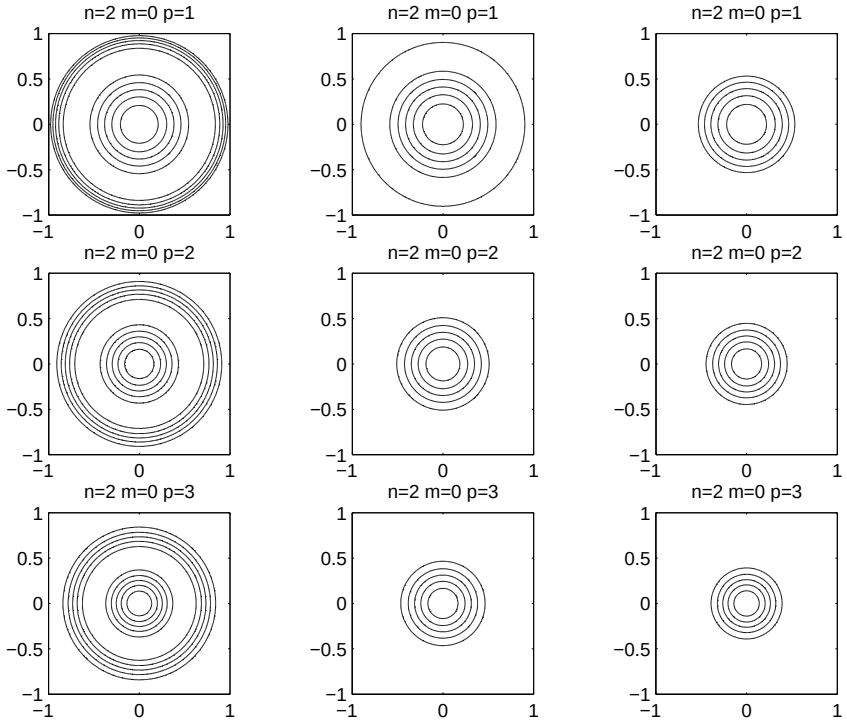

Figure 9: Streamlines for $n = 2$, $m = 0$, $p = 1, 2, 3$ at $z = 0, 0.4, 0.8$. Streamlines for $n = 4$ are similar.

N	J=3	10	20	3	10	20	3	10	20
	$p=1$			$p=2$			$p=3$		
1	-10.0	-9.88	-9.87	-10.0	-9.88	-9.87	-10.0	-9.88	-9.87
10	-10.0	-9.88	-9.87	-10.0	-9.88	-9.87	-10.0	-9.88	-9.87

Table 2: $\Re\{\lambda_{\max}\}$ for $n=2,4$; $m=0$; $p=1,2,3$; any R; DM_{01}.

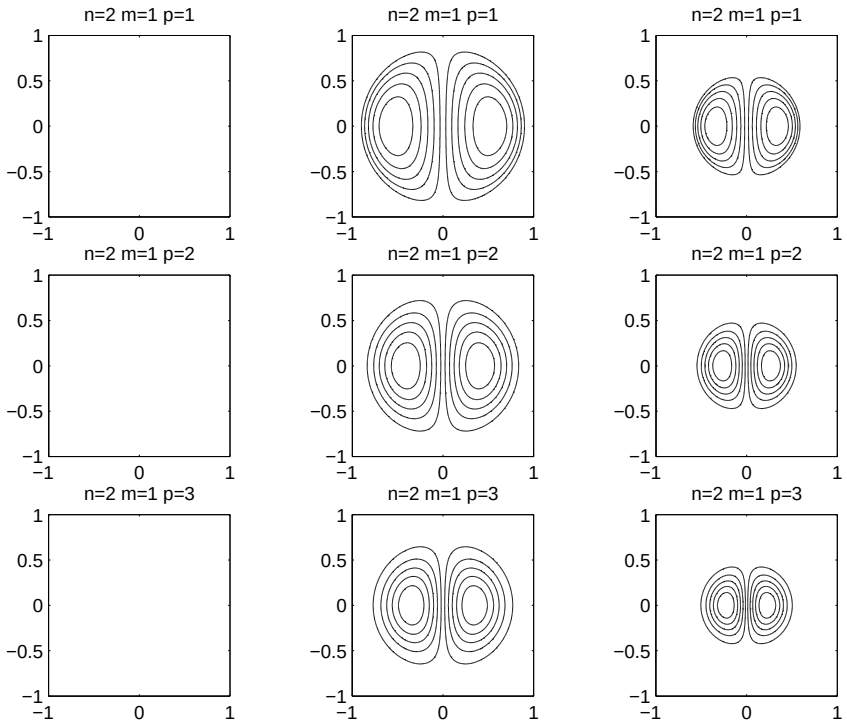

Figure 10: Streamlines for $n=2, m=1, p=1,2,3$ at $z=0, 0.4, 0.8$.

5.1.2 Case $n = 2$, $m = 1$

Figure 10 on the preceding page shows the streamlines for $p = 1, 2, 3$. There is no flow at $z = 0$ because $P_n^m(0) = 0$ when $n - m$ is odd. The flow is divided into two dipolar cells. There is no m-decoupling, so we considered the dipole chain

$$\mathrm{DM}_{01}: \quad S_1^0, S_1^1, T_2^0, T_2^1, T_2^2, S_3^0, S_3^1, S_3^2, S_3^3, T_4^0, T_4^1, T_4^2, T_4^3, T_4^4, \ldots$$

Our results in Table 3 and Figure 11 show that the magnetic field decays faster than the free decay rate $-\pi^2$. So these flows cannot maintain a magnetic field.

N	J=100	200	250	100	200	250	100	200	250
	$p = 1$			$p = 2$			$p = 3$		
9	–26.2	–26.2	–26.2	–18.4	–18.4	–18.4	–17.6	–17.6	–17.6
10	–29.0	–28.8	–28.8	–18.0	–18.0	–18.0	–17.3	–17.3	–17.3
11	–25.0	–25.0	–25.0	–18.3	–18.3	–18.3	–17.4	–17.4	–17.4
12	–24.7	–24.7	–24.7	–18.0	–18.0	–17.9	–17.4	–17.4	–17.4
13	–24.5	–24.7	–24.7	–18.6	–18.6	–18.6	–16.6	–16.8	–16.7
14	–24.9	–24.9	–25.0	–18.4	–18.5	–18.4	–16.4	–16.5	–16.5

Table 3: $\Re\{\lambda_{\max}\}$ for $n = 2$, $m = 1$, $p = 1, 2, 3$; $R = 200$, DM_{01}.

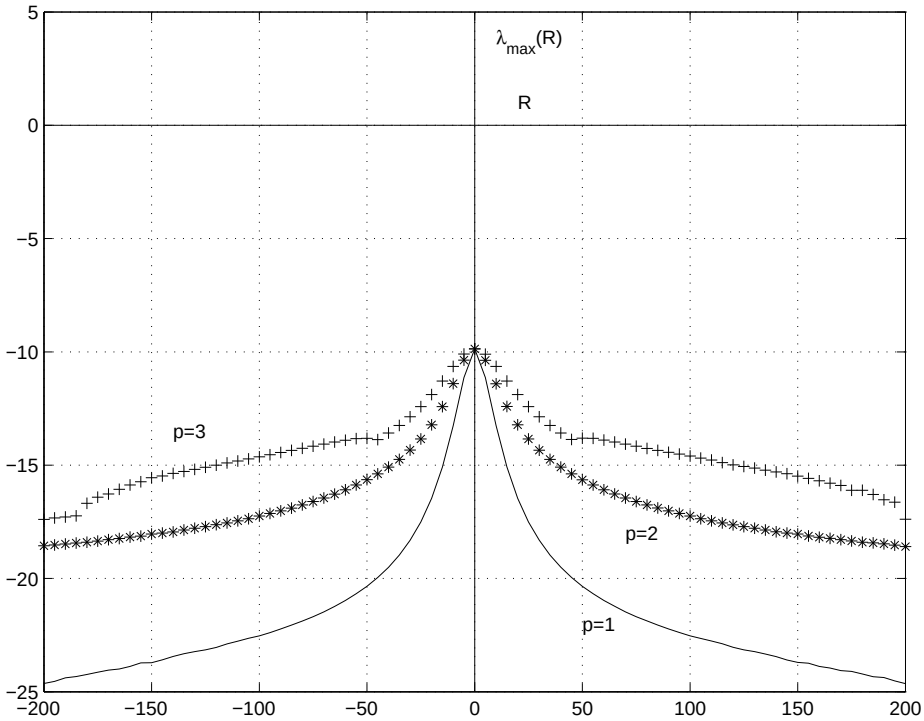

Figure 11: $\Re\{\lambda_{\max}\}$ for $n = 2$, $m = 1$, $p = 1, 2, 3$; DM_{01}, $N = 13$, $J = 250$.

5.1.3 Case $n = 2$, $m = 2$

Figure 12 on the next page shows the streamlines for $n = 2$, $m = 2$ and $p = 1, 2, 3$. The number of cells increases with m, and there is noticeably more shear near the boundary with $p = 1$ than

for $p = 2, 3$. For this flow we first considered the dipole chain

$$\mathrm{DM}_{12}: \quad S_1^1\,, T_2^1\,, S_3^1\,, S_3^3\,, T_4^1\,, T_4^3\,, S_5^1,\ S_5^3,\ S_5^5,\ \ldots$$

and the results are shown in Table 4 on the following page. The flow with $p = 1$ stands out in several respects. Compared to the cases $p = 2, 3$ it is much harder to get convergent results for $p = 1$, the growth rates estimates only starting to settle down above the truncation levels $N \simeq 20$ and $J \simeq 200$. Whilst the level of convergence cannot be regarded as convincing, some $\Re\{\lambda_{\max}\}$ in Table 4 are positive for quite high truncation levels. Thus the $p = 1$ case shows prima facie evidence that it might support magnetic field maintenance. The growth curves at different truncation levels as a function of R_m are shown in Figure 13 on the next page.

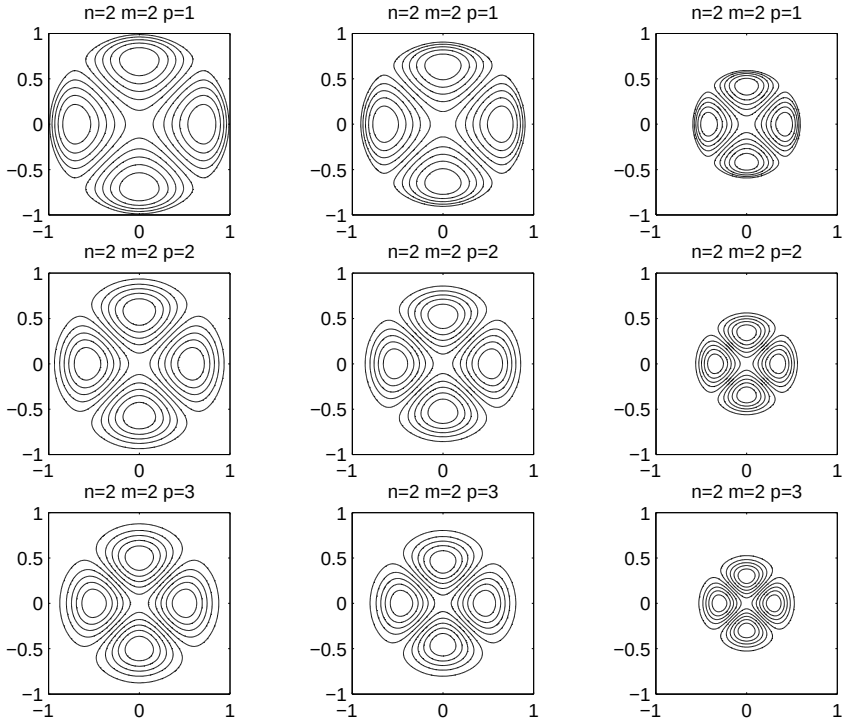

Figure 12: Streamlines for $n = 2$, $m = 2$, $p = 1, 2, 3$, at $z = 0, 0.4, 0.8$.

For this flow we also considered the quadrupole chain

$$\mathrm{QM}_{12}: \quad T_1^1\,, S_2^1\,, T_3^1\,, T_3^3\,, S_4^1\,, S_4^3\,, T_5^1,\ T_5^3,\ T_5^5,\ \ldots$$

and found a similar growing trend, as shown in Figure 14 on page 21.

5.1.4 Case $n = 4$, $m = 1$

Figure 15 on page 21 shows streamlines for $n = 4$, $m = 1$, and $p = 1, 2, 3$. At $z = 0$, there is no flow as $n - m$ is odd. For these flows there is no m-decoupling, so we considered the full dipole chain

$$\mathrm{DM}_{01}: \quad S_1^0\,, S_1^1\,, T_2^0\,, T_2^1\,, T_2^2\,, S_3^0\,, S_3^1\,, S_3^2\,, S_3^3\,, T_4^0\,, T_4^1\,, T_4^2\,, T_4^3\,, T_4^4\,, \ldots$$

All of the growth rates in Table 5 and Figure 16 on page 22 are negative, indicating that the magnetic field decays .

N	J=100	200	250	400	100	200	100	200
		$p=1$			$p=2$		$p=3$	
11	2.01	0.192	–0.028	–0.267	–4.56	–4.77	–12.8	–12.9
12	2.53	–6.11	–7.37	–8.82	–16.7	–16.9	–25.4	–24.8
13	–4.52	–8.94	–9.49	–10.1	–11.2	–11.3	–16.0	–16.1
14	–3.39	–5.99	–6.26	–6.54	–21.8	–22.1	–18.2	–18.3
15	–15.4	–14.6	–14.6	–14.6	–13.1	–13.4	–17.3	–17.4
16	12.3	7.41	6.78	6.08	–14.7	–15.1	–17.4	–17.5
17	2.64	–0.784	–1.22	–1.70	–13.5	–13.9	–17.3	–17.4
18	5.76	0.514	–0.161	–0.907	–14.3	–14.7	–17.3	–17.4
19	–0.817	–6.37	–7.05	–7.78	–14.2	–14.5	–17.4	–17.4
20	7.06	2.40	1.81	1.17	–13.9	–14.3	–17.3	–17.4
21	6.63	1.37	0.702	–0.035	–13.9	–14.3	–17.3	–17.4
22	5.48	0.595	–0.014	–0.681	–14.0	–14.3	–17.3	–17.4
23	4.18	–0.644	–1.25	–1.90	–14.0	–14.4	–17.3	–17.4
24	5.48	0.676	0.745	–0.584	–13.9	–14.3	–17.3	–17.4
25	5.86	0.928	0.308	–0.370	–13.9	–14.3	–17.3	–17.4

Table 4: $\Re\{\lambda_{\max}\}$ for $n=2$, $m=2$, $p=1,2,3$; $R=200$, DM_{12}.

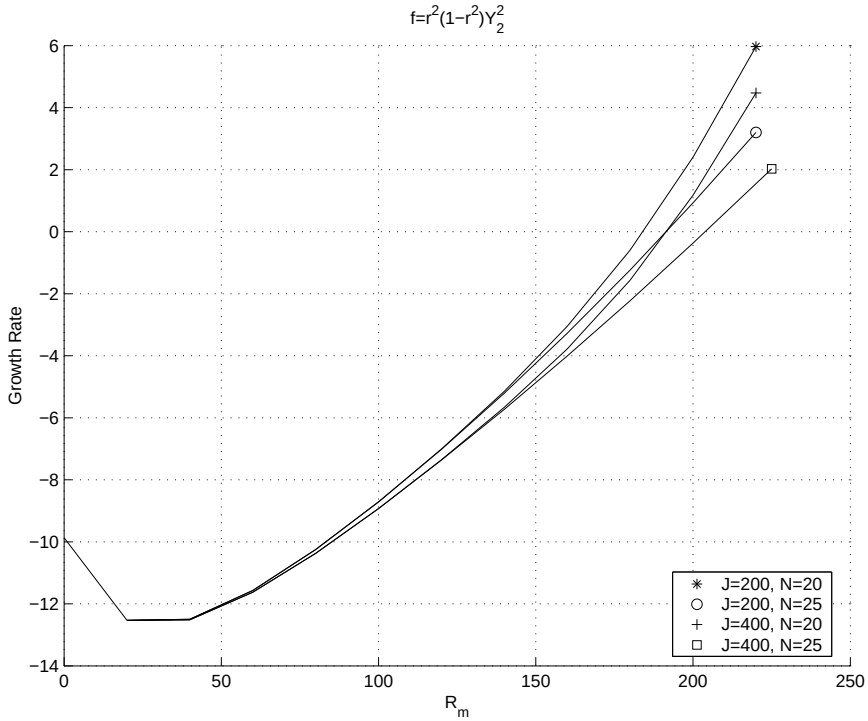

Figure 13: $\Re\{\lambda_{\max}\}$ for $n=2$, $m=2$, $p=1$; DM_{12}; $N=20,25$; $J=200,400$.

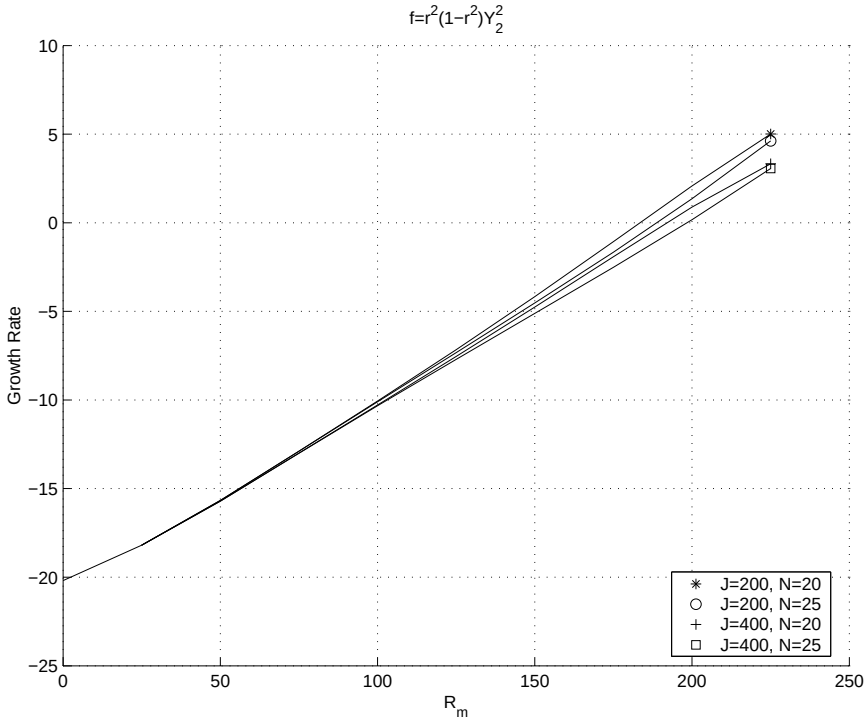

Figure 14: $\Re\{\lambda_{\max}\}$ for $n = 2$, $m = 2$, $p = 1$; QM_{12}; $N = 20, 25$; $J = 200, 400$.

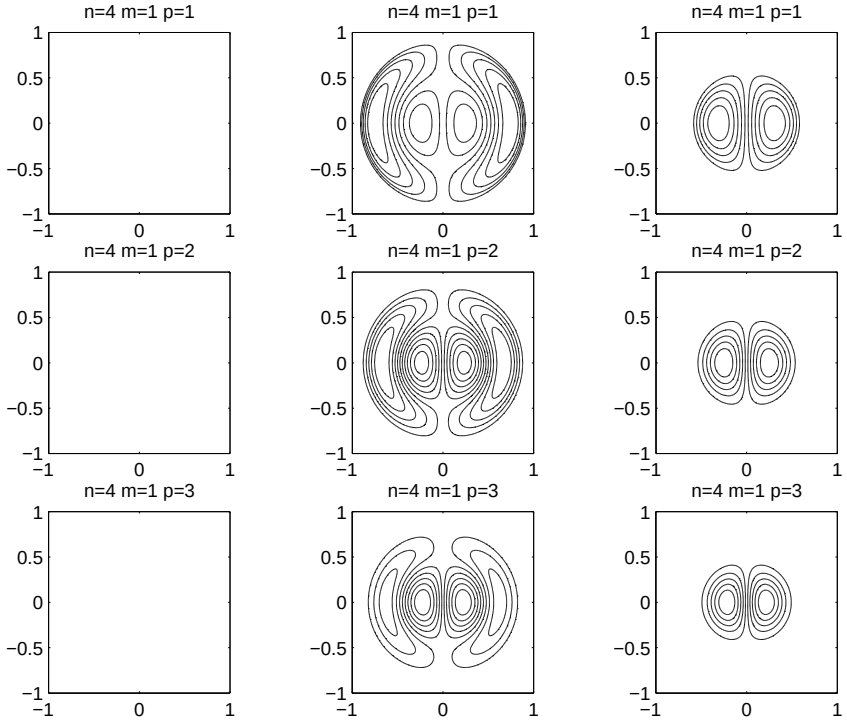

Figure 15: Streamlines for $n = 4, m = 1$ and $p = 1, 2, 3$ at $z = 0, 0.4, 0.8$.

N	J=100	200	250	100	200	250	100	200	250
	$p=1$			$p=2$			$p=3$		
9				-19.9	-19.9	-19.9	-15.5	-15.5	-15.5
10				-19.7	-19.7	-19.7	-15.4	-15.4	-15.4
11	-30.5	-30.7	-30.8	-19.8	-19.9	-19.9	-15.4	-15.4	-15.4
12	-30.5	-30.6	-30.7	-19.8	-19.8	-19.8	-15.4	-15.4	-15.4
13	-31.5	-31.7	-31.8	-19.7	-19.8	-19.8	-15.4	-15.4	-15.4
14	-31.9	-32.2	-32.2	-20.0	-20.0	-20.0	-15.4	-15.4	-15.4
15	-32.8	-33.0	-33.1						

Table 5: $\Re\{\lambda_{\max}\}$ for $n=4$, $m=1$, $p=1,2,3$; $R=200$, DM_{01}.

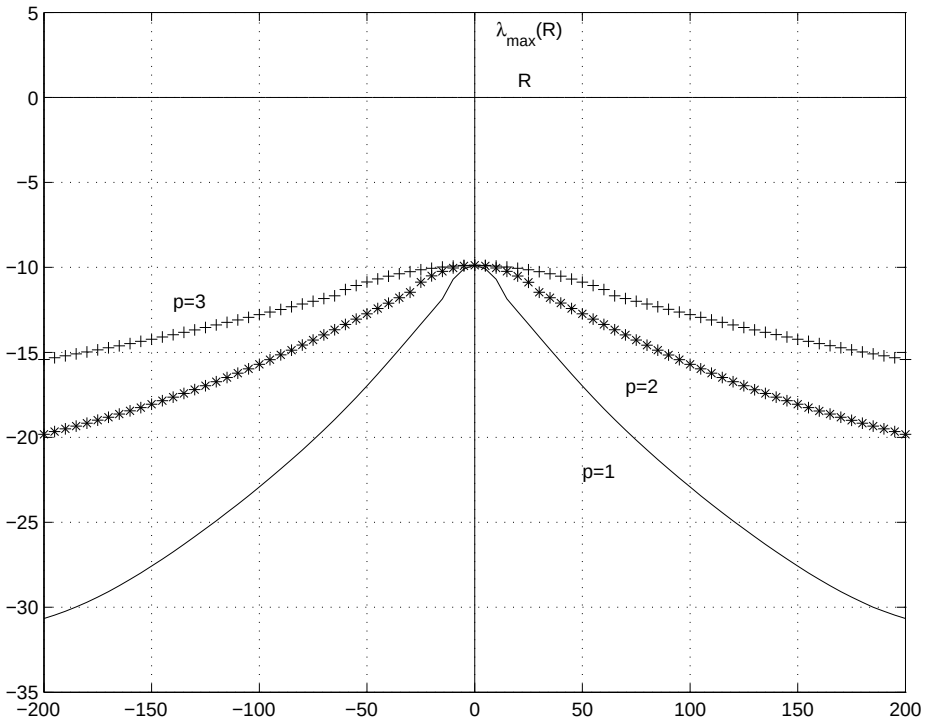

Figure 16: $\Re\{\lambda_{\max}\}$ for $n=4$, $m=1$, $p=1,2,3$; $N=12$, $J=250$,, M_{01}.

5.1.5 Case $n = 4$, $m = 2$

Figure 17 shows streamlines for $n = 4$, $m = 2$ and $p = 2, 3$. We used the dipole chains

$$\begin{aligned} \mathrm{DM}_{02}: &\quad S_1^0, T_2^0, T_2^2, S_3^0, S_3^2, T_4^0, T_4^2, T_4^4, S_5^0, S_5^2, S_5^4, \ldots && \text{for } p = 2 \\ \mathrm{DM}_{12}: &\quad S_1^1, T_2^1, S_3^1, S_3^3, T_4^1, T_4^3, S_5^1, S_5^3, S_5^5, \ldots && \text{for } p = 3 \end{aligned}$$

Results are shown only for $p = 2, 3$. Convergence was not obtained for $p = 1$ at the same N, J levels, and higher truncations await investigation. Table 6 and Figure 18 on the next page again support the Planar Velocity Theorem. Table 6 again shows it is easier to get convergent results when there is lower shear near the boundary, i.e. higher p.

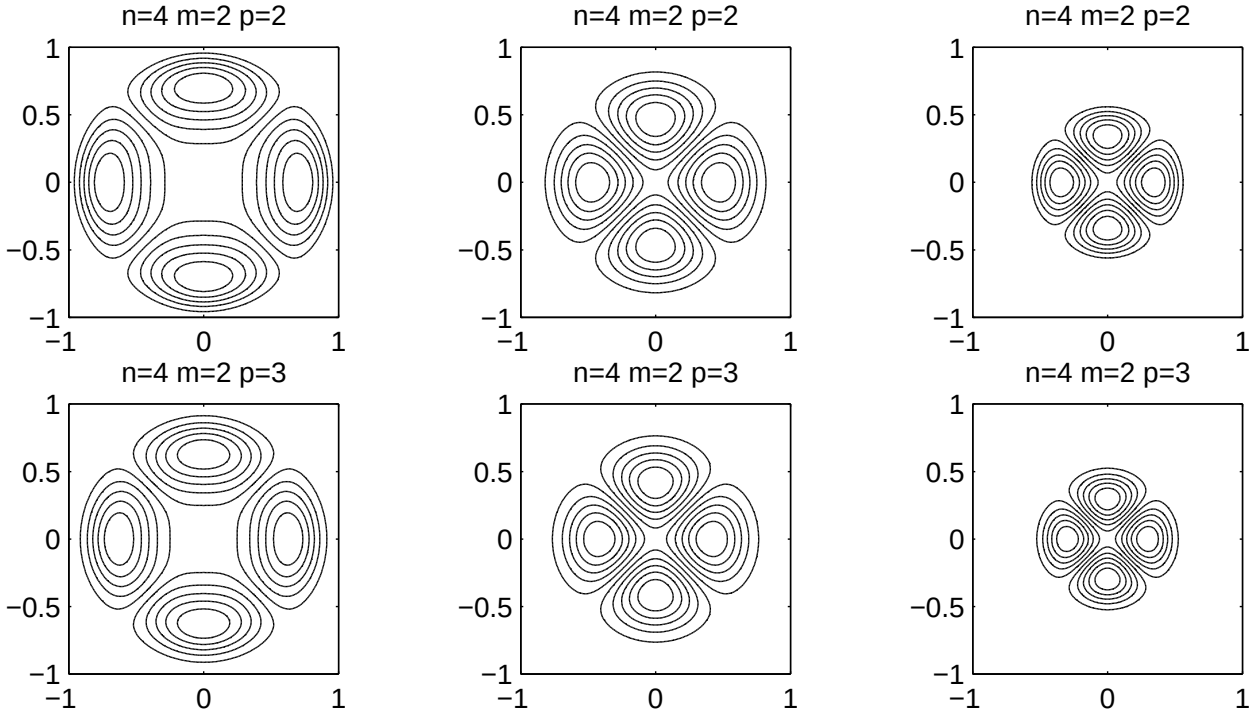

Figure 17: Streamlines $n = 4, m = 2$ and $p = 2, 3$, at $z = 0, 0.4, 0.8$.

N	J=100	200	250	100	200	250
	$p = 2\,(\mathrm{DM}_{12})$			$p = 3\,(\mathrm{DM}_{02})$		
9	–16.7	–16.7	–16.7	–17.0	–17.0	–17.0
10	–21.3	–25.5	–25.5	–18.0	–18.0	–18.0
11	–21.4	–21.5	–21.5	–18.0	–18.0	–18.0
12	–19.5	–19.5	–19.5	–17.8	–17.8	–17.8
13	–21.1	–21.1	–21.1	–18.0	–18.0	–18.0
14	–23.3	–23.4	–23.4	–18.0	–18.0	–18.0

Table 6: $\Re\{\lambda_{\max}\}$ for $n = 4$, $m = 2$, $p = 2\,(\mathrm{DM}_{12})$, $p = 3\,(\mathrm{DM}_{02})$, $R = 200$.

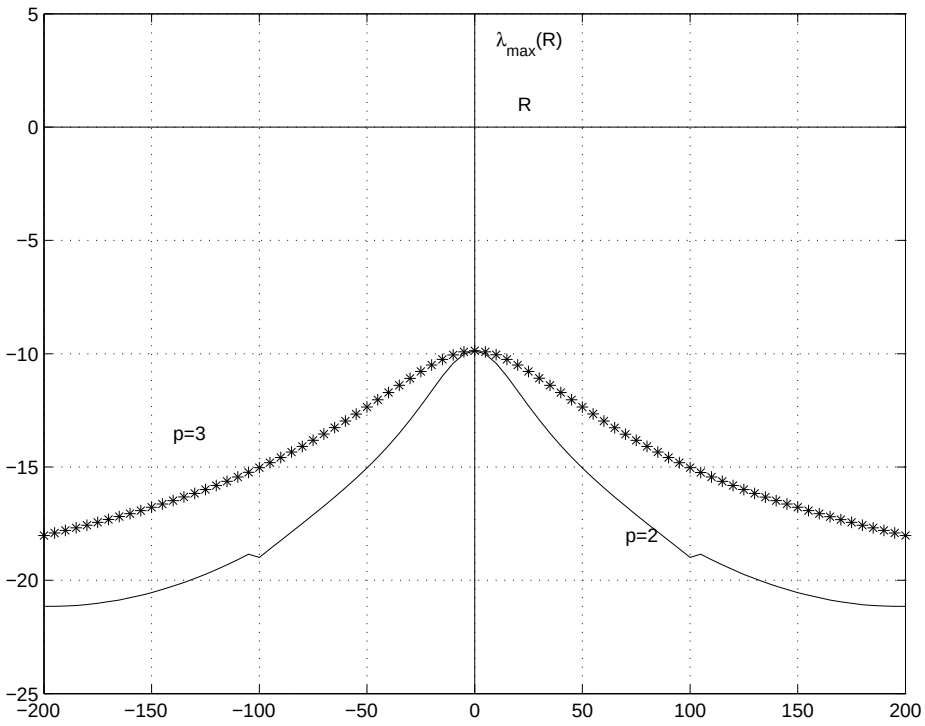

Figure 18: $\Re\{\lambda_{\max}\}$ for $n = 4$, $m = 2$, $p = 2\,(\mathrm{DM}_{12})$, $p = 3\,(\mathrm{DM}_{02})$, $N = 13, J = 250$.

5.1.6 Case $n = 4$, $m = 3$

Figure 19 on the next page shows streamlines for $n = 4$, $m = 3$ and $p = 2, 3$. At $z = 0$, there is no flow as $n - m$ is odd. We used the dipole chain

$$\mathrm{DM}_{13}: \quad S_1^1\,, T_2^1\,, S_3^1\,, S_3^3\,, T_4^1\,, T_4^3\,, S_5^1,\ S_5^3,\ S_5^5,\ \ldots$$

No convergent results were obtained for $p = 1$. Table 7 and Figure 20 on the next page again show that all growth rates are negative.

N	J=100	200	250	100	200	250
	$p = 2$			$p = 3$		
9	–12.6	–12.7	–12.7	–16.3	–16.3	–16.3
10	–23.4	–23.4	–23.4	–17.0	–17.0	–17.0
11	–19.8	–20.0	–20.0	–17.5	–17.5	–17.5
12	–21.8	–21.8	–21.9	–17.9	–17.9	–17.9
13	–19.5	–19.6	–19.6	–17.1	–17.1	–17.1
14	–19.3	–19.4	–19.4	–17.4	–17.4	–17.4

Table 7: $\Re\{\lambda_{\max}\}$ for $n = 4$, $m = 3$, $p = 2, 3$; $R = 200$, DM_{13}.

5.1.7 Case $n = 4$, $m = 4$

Figure 21 on page 26 shows streamlines for $n = 4$, $m = 4$, and $p = 1, 2, 3$. We used the chain

$$\mathrm{DM}_{14}: \quad S_1^1\,, T_2^1\,, S_3^1\,, S_3^3\,, T_4^1\,, T_4^3\,, S_5^1\,, S_5^3\,, S_5^5\,, \ldots$$

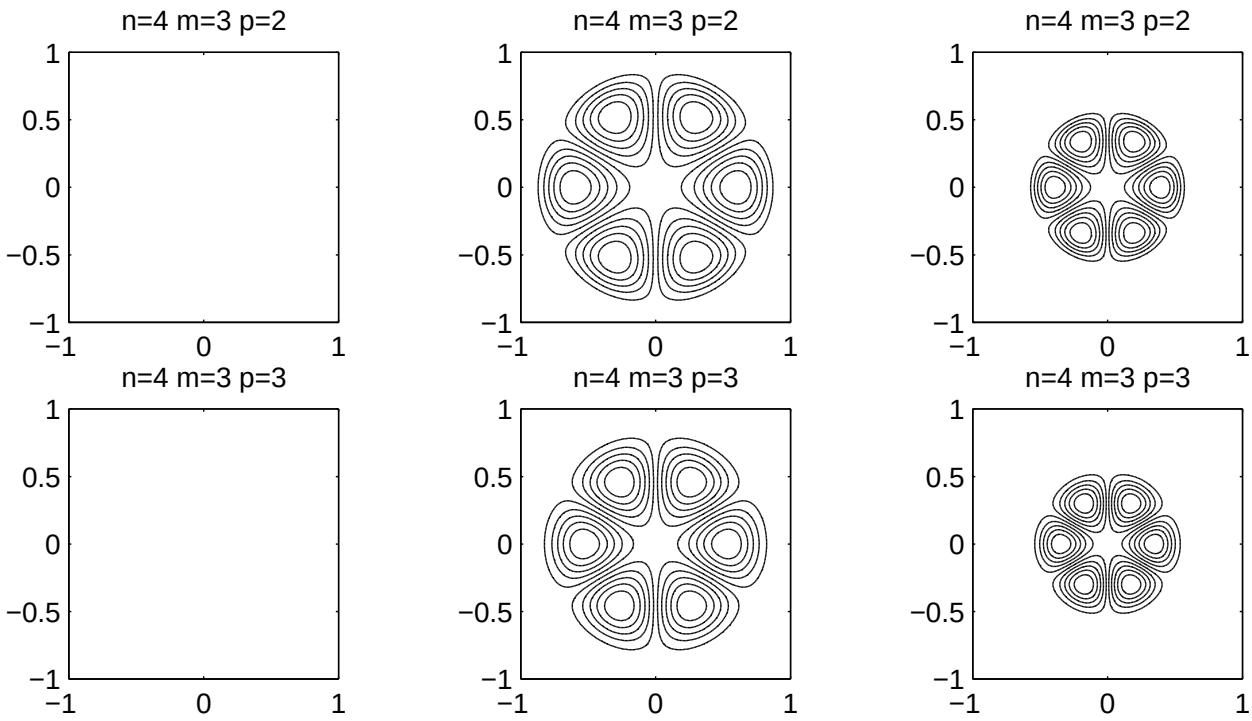

Figure 19: Streamlines for $n = 4, m = 3$ and $p = 2, 3$ at $z = 0, 0.4, 0.8$.

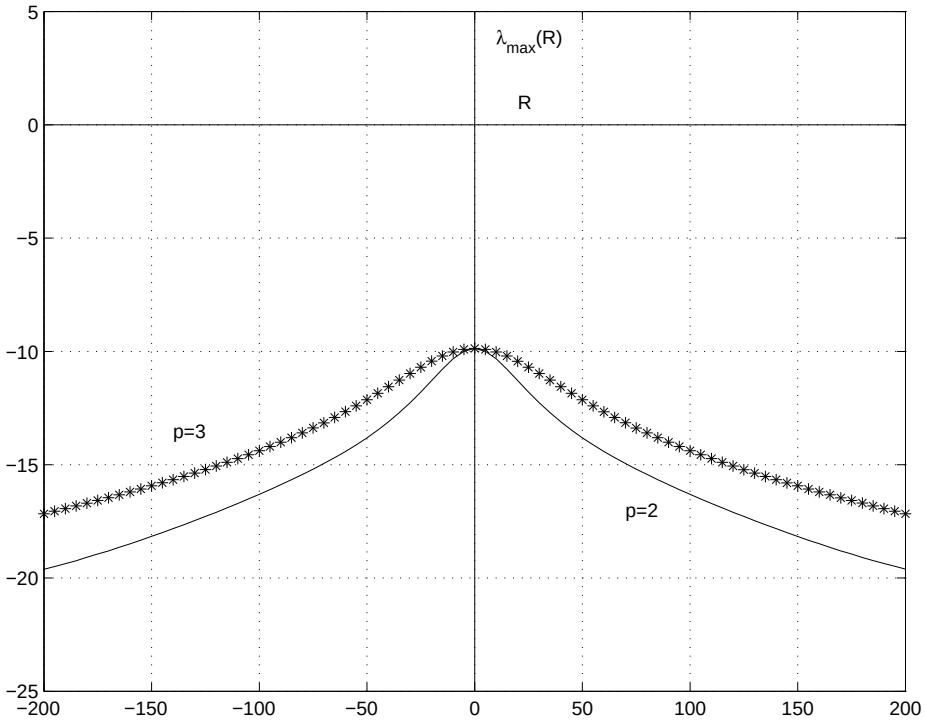

Figure 20: $\Re\{\lambda_{\max}\}$ for $n = 4$, $m = 3$, $p = 2, 3$; DM_{13}, $N = 13$, $J = 250$.

These flows have high shear away from the z-axis, and convergence has not been achieved for $p = 1$. The only inference to be made from Table 8 is that all the growth rates are negative.

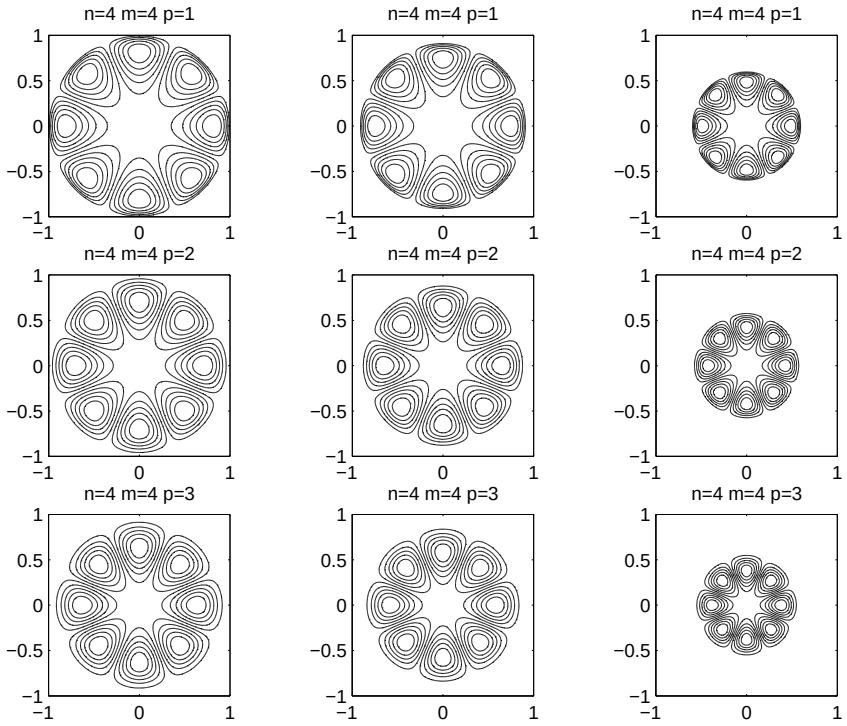

Figure 21: Streamlines for $n = 4$, $m = 4$, $p = 1, 2, 3$ at $z = 0, 0.4, 0.8$.

N	J=100	200	250	100	200	250	100	200	250
		$p = 1$			$p = 2$			$p = 3$	
11	44.1	35.1	34.3	−15.7	−16.0	−15.9	−15.0	−15.0	−15.0
12	−16.9	10.9	10.1	−18.0	−18.1	−18.1	−15.4	−15.4	−15.4
13	−11.5	−17.3	−18.0	−20.0	−20.1	−20.1	−15.7	−15.7	−15.7
14	−9.34	−23.0	−23.8	−19.4	−19.5	−19.5	−15.9	−15.9	−15.9

Table 8: $\Re\{\lambda_{\max}\}$ for $n = 4$, $m = 4$, $p = 1, 2, 3$; $R = 200$, DM_{14}.

5.2 Planarizing some classic flows

In this section we consider planarizing three classic flow models using the method of §4. In two of the three cases it is not possible to planarize, for two different reasons. In one case, part planarization is possible, but destroys the pre-existing field growth.

5.2.1 Bullard-Gellman flow

In the present formalism the classic Bullard-Gellman flow ([1] is given by

$$\mathbf{v} = \epsilon \mathbf{t}_1^0 + \mathbf{s}_2^2 + \mathbf{s}_2^{-2} \,, \tag{48}$$

where

$$t_1^0 = \tfrac{1}{\sqrt{3}}\, r(1-r)\ , \qquad s_2^2 = s_2^{-2} = \sqrt{\tfrac{6}{5}}\, r^2(1-r)^2\ .$$

A planarized version of the BG flow is

$$\mathbf{v} = \epsilon \mathbf{t}_1^0 + 2\Re\left\{\mathbf{s}_2^2 + \mathbf{t}_3^2\right\}\ . \tag{49}$$

From (40) and (44b),

$$t_3^2 = -\tfrac{1}{4\sqrt{7}}\left(\frac{df_2}{dr} - \frac{3}{r}\, f_2\right)$$

where $f_2 = i\, s_2^2/3 = i\,\sqrt{(2/5)}\, r^2(1-r)^2$. Since the BG flow does not function as a dynamo, we have not pursued its planarized version numerically, but merely give it above as an example of a flow that is easily planarized.

5.2.2 Kumar-Roberts flow

The Kumar-Roberts flow (50) was one of the first shown to function as a dynamo [15]. It evolved from the Bullard-Gellman flow (48) by the addition of the large scale meridional circulation s_2^0. It is a convenient flow to consider because of its fast numerical convergence. Here

$$\mathbf{v} = \mathbf{t}_1^0 + \epsilon_1 \mathbf{s}_2^0 + \epsilon_2 \mathbf{s}_2^2 + \epsilon_3 \mathbf{s}_2^{-2}\ , \tag{50}$$

where

$$t_1^0 = \frac{r(1-r^2)}{\sqrt{3}}\ , \quad s_2^0 = \frac{r^5(1-r^2)^3}{\sqrt{5}}\ , \quad s_2^2 = \overline{s_2^{-2}} = \frac{r^3(1-r^2)^2 e^{-ipr} i}{\sqrt{10}}\ .$$

This motion satisfies the fixed boundary condition (34) and no-slip conditions (35), but not the differentiability condition (33). We used $\epsilon_1 = 0.03$, $\epsilon_2 = \epsilon_3 = 0.04$, $p = 3\pi$, values known to produce dynamo action [15]. This flow cannot be fully planarized using (40), since $m = 0$ for the meridional circulation $\mathbf{s}_2^0$. Removing s_2^0 would just revert to a Bullard-Gellman type flow (48), and not auger well for a growing field. We thus left $\mathbf{s}_2^0$ unchanged, and investigated the effect of just planarizing the s_2^2 component. This was done by the addition of a t_3^2 component as in §5.2.1. The end result is a meridional flow $\mathbf{s}_2^0$ superimposed on a planar flow $\mathbf{s_2^2} + \mathbf{t}_1^0 + \mathbf{t}_3^2$.

From (40) and s_2^2 in (50), we find

$$f_2 = \frac{3r^3(1-r^2)^2 e^{-ipr}}{\sqrt{10}}. \tag{51}$$

Equation (44) then gives the corresponding t_3^2 that planarizes s_2^2, noting $t_1^2 \equiv 0$. As shown by our numerical results in Figure 22 on the following page this part planarization greatly flattens the growth curve, and removes the possibility of dynamo action. Although not shown on the graph, this rapid decay persisted even though we increased the magnetic Reynolds number out to 5000.

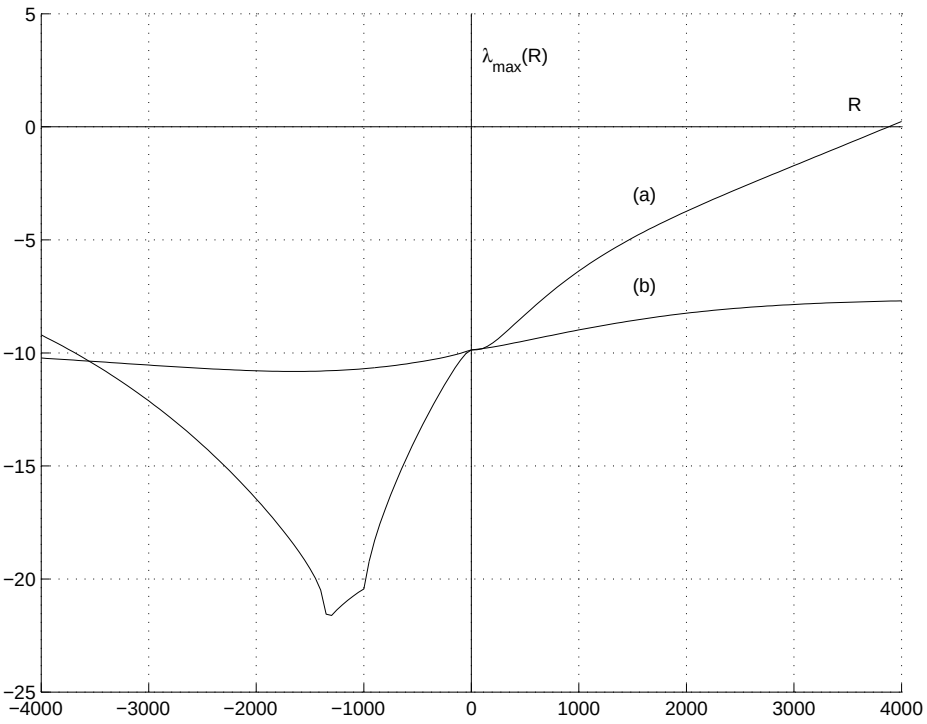

Figure 22: $\Re\{\lambda_{\max}\}$ for (a) the Kumar-Roberts flow, and (b) the partly planarized Kumar-Roberts flow, using $N = 12$, $J = 250$.

5.3 Pekeris, Accad, and Shkoller flow

Lastly we consider the possibility of planarizing the Pekeris, Accad, and Shkoller (PAS) flow, another early successful kinematic dynamo [20]. We give this as an example that it is not always possible to planarize a flow even when it has no axisymmetric meridional component. The motion of PAS is

$$\mathbf{v} = 2\Re\{\mathbf{s}_2^2 + \mathbf{t}_2^2\}, \tag{52}$$

where

$$s_2^2 = k\Lambda j_2(\Lambda r) \ , \qquad t_2^2 = k\Lambda s_2^2(r) \ .$$

Here $k = \sqrt{6/5}$, and Λ is a positive root of the spherical Bessel function

$$j_2(x) = \left(\frac{3}{x^3} - \frac{1}{x}\right)\sin x - \frac{3}{x^2}\cos x \ .$$

From (40), $\mathbf{s}_2^2$ in (52) is planarized by using

$$f_2^2 = -3ik\Lambda j_2(\Lambda r) \ ,$$

and then obtaining t_3^2 from (44b). However, for $\mathbf{t}_2^2$ in (52), since $f_1^2 \equiv 0$, a planarizing f_3^2 must be found from (44a), by solving

$$t_2^2 = \frac{1}{3}\alpha_3 \frac{df_3^2}{dr} + \frac{4}{3r} f_3^2 \ . \tag{53}$$

Since t_2^2 does not satisfy (45a), it is not possible to find f_3^2 satisfying both the differentiability condition (33) and the fixed boundary condition (34).

6 Conclusions

In §2 the Planar Velocity Theorem was reviewed , and in §2.2 it was argued that the proof fails due to diffusive coupling of the horizontal and vertical fields $\mathbf{B}_h$ and B_z. In §4 the relations between the stream function for a planar flow and the spherical harmonic poloidal and toroidal spectral components were derived. The spectral equations given in §3.1 form the basis for a numerical investigation of possible field maintenance by planar flows. In §5 we have reported on the numerical growth rates determined for a number of single degree planar flows $\mathbf{v} = \nabla\times(f\mathbf{e}_z) = 2\Re\{\mathbf{s}_n^m + \mathbf{t}_{n+1}^m + \mathbf{t}_{n-1}^m\}$ using stream functions $f = r^n(1-r^2)^p\, Y_n^m$. All of our results, where convergence was obtained, indicate field decay, except for the case $n = m = 2, p = 1$. As shown by Figures 13 and 14 on page 20, the λ-curves for this flow behave remarkably differently from all others, the latter typified by the decay results in Figure 11 on page 18. Figures 13 and 14 are prima facie evidence that planar flows can maintain magnetic fields. However, a more definite conclusion can not be made since convergence has not yet been attained to a level that removes all doubt. Such convergence requires either larger computing resources, or an alternative numerical approach.

At the outset of this project, and given formula (12), it was expected that lower p and hence higher velocity shear near the boundary, would be more effective in acting as a self sustaining dynamo. Superficially, this has proven true in that the most probably successful candidate is the stream function $f = r^2(1-r^2)^p\, Y_2^2$ with $p = 1$. However, in other cases flows with higher p have produced slower decay rates, making it not possible to make a conclusion about effectiveness based simply on p. For example, see Figure 11 on page 18 where the $p = 1$ flow produces the most rapidly decaying magnetic field.

For the Earth, rotation is a very significant factor. Fully dynamical geodynamo models [6] show concentrations of planar flow, indeed zonal flow, about the inner core boundary and extending into the tangent cylinder above and below the inner core. Thus the study of the efficacy of planar flows is of considerable interest. The resolution of the convergence difficulties referred to above, and the establishment of the validity or otherwise of the Planar Velocity Theorem remain the subject of ongoing work.

Acknowledgements:

One of us (AAB) wishes to acknowledge financial support from an Australian Development Scholarship at the University of Sydney, whilst on leave from the University of Indonesia. Some of our results were generated using the Sydney Regional Visualisation Laboratory which is supported by the Australian Research Council.

References

[1] E.C. Bullard and H. Gellman, 1954, Homogenous dynamos and terrestrial magnetism, *Phil. Trans. R. Soc. Lond. A* **247**, 213–278.

[2] S. Chapman and J. Bartels, *Geomagnetism*, Oxford University Press, Vol II, 1962.

[3] U.R. Christensen, J. Aubert, P. Cardin, E. Dormy, S. Gibbons, G.A. Glatzmaier, E. Grote, Y. Honkura, C. Jones, M. Kono, M. Matsushima, A. Sakuraba, F. Takahashi, A. Tilgner,

J. Wicht, K. Zhang, 2001, A numerical dynamo benchmark, *Phys. Earth Plan. Int.* **128**, 25–34.

[4] T.G. Cowling, 1957, The dynamo maintenance of steady magnetic fields, *Q. Jnl. Mech. App. Math.* **10**, 129–136.

[5] M.L. Dudley and R.W. James, 1989, Time-dependent kinematic dynamos with stationary flows, *Proc. R. Soc. Lond. A* **425**, 407–429.

[6] G.A. Glatzmaier, 1997, *Core Convection and the Geodynamo*, http://ees-www.lanl.gov/IGPP/Geodynamo.html.

[7] D.J Ivers and R.W. James, 1984, Axisymmetric antidynamo theorems in compressible non-uniform conducting fluids, *Phil. Trans. R. Soc. Lond.*, **312**, 179–218.

[8] D.J Ivers and R.W. James, 1986, Extension of the Namikawa-Matsushita antidynamo theorem to toroidal fields, *Geophys. Astrophys. Fluid Dynamics*, **36**, 317–324.

[9] D.J. Ivers and R.W. James, 1988, Antidynamo theorems for non-radial flows, *Geophys. Astrophys. Fluid Dynamics*, **40**, 147–163.

[10] D.J. Ivers and R.W. James, 1988, An Antidynamo Theorem for Partly Symmetric Flows, *Geophys. Astrophys. Fluid Dynamics*, **44**, 271–278.

[11] R.W. James, 1973, The Adams and Elsasser dynamo integrals, *Proc. R. Soc. Lond. A*, **331**, 469–478.

[12] R.W. James, 1974, The spectral form of the magnetic induction equation, *Proc. R. Soc. Lond. A*, **340**, 278–299.

[13] R. Kaiser, 1995, Towards a poloidal magnetic field theorem, Geophys. Astrophys. Fluid Dynamics 80, 93-109 (1995).

[14] R. Kaiser, B.J. Schmitt and F.H. Busse, 1994, On the invisible dynamo, *Geophys. Astrophys. Fluid Dynamics*, **44**, 271–278.

[15] S. Kumar and P.H. Roberts, 1975, A three-dimensional kinematic dynamo, *Proc. R. Soc. Lond. A*, **344**, 235–258.

[16] J. Larmor, 1919, How could a rotating body such as the sun become a magnet? *Rep. Brit. Ass. Advmt. Sci.* **4**, 159–160.

[17] J.J. Love and D. Gubbins, 1996, Dynamos driven by poloidal flow exist, *Geophys. Res. Letters* **23**, 857–860.

[18] T. Namikawa and S. Matsushita, 1970, Kinematic dynamo problem, *Geophys. J. R. Astr. Soc.*, **19**, 395–415.

[19] H.K. Moffatt *Magnetic Field Generation in Electrically Conducting Fluids* Cambridge University Press, 1978, p.122.

[20] C.L. Pekeris, Y. Accad, B. Shkoller, 1973, Kinematic dynamos and the Earth's magnetic field, *Proc. R. Soc. Lond. A*, **275**, 425–261.

[21] J. H. Wilkinson, *The Algebraic Eigenvalue Problem*, Oxford : Clarendon Press 1965.

[22] Ya.b. Zel'dovitch, A.A. Ruzmaikin, 1980, The magnetic field in a conducting fluid in two-dimensional motion, *JETP*,]textbf51, 493–497.